

# Quantifying Eulerian Eddy Leakiness in An Idealized Model

**Tongya Liu** (liutongya@sio.org.cn)

Ocean College, Zhejiang University, Zhoushan, Zhejiang, China

& State Key Laboratory of Satellite Ocean Environment Dynamics, Second Institute of Oceanography,  
Hangzhou, Zhejiang, China

**Ryan Abernathey** (rpa@ldeo.columbia.edu)

Lamont-Doherty Earth Observatory, Columbia University, New York, NY, USA

**Anirban Sinha** (as4479@columbia.edu)

California Institute of Technology, Pasadena, CA, USA

**Dake Chen** (dchen@sio.org.cn)

State Key Laboratory of Satellite Ocean Environment Dynamics, Second Institute of Oceanography,  
Hangzhou, Zhejiang, China

This manuscript is a preprint. We have submitted this paper to JGR-OCEANS, and it has yet to be accepted. Please feel free to contact any of the authors directly. We welcome any suggestion and feedback.

# Quantifying Eulerian Eddy Leakiness in An Idealized Model

Tongya Liu<sup>1,2</sup>, Ryan Abernathey<sup>3</sup>, Anirban Sinha<sup>4</sup>, and Dake Chen<sup>2</sup>

<sup>1</sup>Ocean college, Zhejiang University, Zhoushan, Zhejiang, China

<sup>2</sup>State Key Laboratory of Satellite Ocean Environment Dynamics, Second Institute of Oceanography, Ministry of Natural Resources, Hangzhou, Zhejiang, China

<sup>3</sup>Lamont-Doherty Earth Observatory, Columbia University, New York, NY, USA

<sup>4</sup>California Institute of Technology, Pasadena, CA, USA

## Key Points:

- SSH eddies overestimate coherent core and fail to reveal more than half of Lagrangian eddies
- The leakage of SSH eddies reach more than 50% over the lifetime
- About half of SSH eddies are not significantly different from random ocean pieces in material coherence

## Abstract

An idealized eddy-resolving ocean basin, closely resembling the North Pacific ocean, is simulated using MITgcm. We identify rotationally coherent Lagrangian vortices (RCLVs) and sea surface height (SSH) eddies based on the Lagrangian and Eulerian framework, respectively. General statistical results show that RCLVs have a much smaller coherent core than SSH eddies with the ratio of radius is about 0.5. RCLVs are often enclosed by SSHA contours, but SSH eddy identification method fails to detect more than half of RCLVs. Based on their locations, two types of eddies are classified into three categories: overlapping RCLVs and SSH eddies, non-overlapping SSH eddies, and non-overlapping RCLVs. Using Lagrangian particles, we examine the processes of leakage and intrusion around SSH eddies. For overlapping SSH eddies, over the lifetime, the material coherent core only accounts for about 25%, and about 50% of initial water leak from eddy interior. The remaining 25% of water can still remain inside the boundary, but only in the form of filaments outside the coherent core. For non-overlapping SSH eddies, more water leakage (about 60%) occurs at a faster rate. Guided by the number and radius of SSH eddies, fixed circles and moving circles are randomly selected to diagnose the material flux around these circles. We find that the leakage and intrusion trends of moving circles are quite similar to that of non-overlapping SSH eddies, suggesting that the material coherence properties of non-overlapping SSH eddies are not significantly different from random pieces of ocean with the same size.

## Plain Language Summary

Material coherent transport is widely estimated based on the Eulerian methods, but the organization of Eulerian eddies determines Eulerian eddies can not keep material coherence during the lifespan. In this study, we examine the relationship between eddy detection methods and material coherent transport, and quantitatively estimate the Eulerian eddy leakiness in material transport. We compare the statistical features of RCLVs and SSH eddies identified from a high-resolution idealized model based on two different frameworks. We find that the Eulerian method fails to detect many Lagrangian structures and overestimate the real coherent core. Besides, using Lagrangian particles, we quantify the material flux across SSH eddies boundaries. Our results suggest that SSH eddies are far from coherent structures, with the leakage of initial water reach at least 50%. We also find that one type of SSH eddies are not significantly different from random pieces of ocean with the same size in material coherence properties. Our findings suggest that using Eulerian eddy boundaries to estimate coherent transport may be misleading.

## 1 Introduction

Mesoscale eddies with horizontal spatial scales broadly between tens and a few hundred kilometers are ubiquitous structures in the ocean (*Fu et al.* [2010]), transporting and redistributing mass, heat, salt, potential vorticity, and other biochemical tracers throughout the ocean. This transport is believed to have significant impacts on the large-scale ocean circulation, marine ecosystems, and long-term earth climate (e.g. *Jayne and Marotzke* [2001]; *Dong et al.* [2014]; *Zhang et al.* [2014]; *Gaube et al.* [2015]; *Griffies et al.* [2015]; *Kouketsu et al.* [2016]). Understanding the degree of coherent eddy transport is a key issue for more accurate parameterization of mesoscale transport in coarse-resolution climate models. Here “coherent eddy transport” refers to the water trapping process, in which material transport barriers prevent effective water exchange between the eddy interior and background flows over a finite time interval (*Frenger et al.* [2015]; *Haller and Beron-Vera* [2013]; *Haller* [2015]). However, a survey of previous studies reveals that estimates of coherent eddy transport based on different identification methods vary dramatically. In this paper, we aim to clarify the relationship between eddy identification methods and material coherent transport. Also, we seek to examine the extent to which the eddies detected by different methods maintain coherence over their lifetimes.

A number of methods have been employed to identify coherent eddies. We review these methods in two categories: Eulerian methods, based on instantaneous information of the flow field, and

63 Lagrangian methods, based on water parcel trajectories over a finite time interval. The fundamental  
64 concept of Eulerian methods is to identify the eddy boundary through anomaly contours of some  
65 instantaneous Eulerian field, and then track these boundaries on the basis of their geographic locations  
66 at a proximate time. The Eulerian fields used to define the ocean eddy boundaries include Okubo-  
67 Weiss (OW) parameter (*Okubo* [1970]; *Weiss* [1991]; *Isern-Fontanet et al.* [2003]), Geometry-based  
68 method (*Chaigneau et al.* [2008]); sea surface height (SSH; *Chelton et al.* [2011]; *Faghmous et al.*  
69 [2015]), velocity streamlines (*Nencioli et al.* [2010]), sea surface temperature (*Dong et al.* [2011];  
70 *Hausmann and Czaja* [2012]), and potential vorticity (*Zhang et al.* [2014]). Due to their relative  
71 computational simplicity, the Eulerian methods have been more widely used in the oceanography  
72 community, especially the eddy census of *Chelton et al.* [2011] derived from satellite altimetry.

73 Eulerian eddy detection has many valuable applications. However, several shortcomings of  
74 Eulerian detection methods (discussed by *Haller* [2015] and *Peacock et al.* [2015]) must be considered  
75 in the context of eddy transport. First, the Eulerian methods are not objective; material transport  
76 should not depend on the choice of reference frame, but Eulerian eddies may change dramatically  
77 when the reference frame changes (e.g. via translation or rotation). Second, the boundary of the  
78 Eulerian eddy is not material; the contours in scalar field do not represent persistent material  
79 barriers that forbid material exchange. That means the water inside Eulerian eddy boundaries is not  
80 necessarily the same fluid at different times. In addition, the choice of numerous parameters and  
81 thresholds is another inevitable drawback of Eulerian methods. In contrast, Lagrangian coherent  
82 structures derived from Lagrangian fluid motion are a natural choice for assessing coherent eddy  
83 transport, since they are material by construction. Recently, several different methods, including  
84 finite-time Lyapunov exponents (FTLE; *Beron-Vera et al.* [2008]), finite-scale Lyapunov exponent  
85 (FSLE; *dÓvidio et al.* [2009]), geodesic transport barriers (*Haller and Beron-Vera* [2013]; *Beron-*  
86 *Vera et al.* [2013, 2015]), and Lagrangian-averaged vorticity deviation (LAVD; *Haller et al.* [2016]),  
87 have been introduced to reveal materially coherent ocean eddies.

88 Among numerous studies to estimate material coherent transport based on Eulerian identification  
89 methods, the following two have received considerable attention due to their global scope and  
90 surprising results. Under the framework of Eulerian eddy detection, *Dong et al.* [2014] combined  
91 Argo profile data and a velocity-based Eulerian eddy dataset to estimate horizontal heat and salt  
92 transports due to coherent eddy translation. They concluded that most of the eddy transport in the  
93 ocean is due to individual eddy movements. *Zhang et al.* [2014] defined the eddy boundary via  
94 the outermost closed potential vorticity contour and conducted a similar calculation for eddy mass  
95 transport. They found that the zonal westward mass flux induced by eddies in the subtropical gyres  
96 can reach about 30 Sv, which is comparable to the wind-driven transport.

97 However, several works using Lagrangian frameworks have presented quite conflicting results.  
98 For instance, *Abernathey and Haller* [2018] adopted the Lagrangian-averaged vorticity deviation  
99 method of *Haller et al.* [2016] to detect eddies in the eastern Pacific and quantified the contribution  
100 of coherent transport to total transport. They found that the coherent meridional transport accounted  
101 for less than 1% of the total flux, and the incoherent part, including chaotic stirring and filamentation  
102 outside of eddy cores, was the dominant mechanism for eddy transport. Similarly, the work of  
103 *Beron-Vera et al.* [2013], *Froyland et al.* [2015]) and *Wang et al.* [2015, 2016] examined the ability  
104 of Agulhas rings to coherently carry Agulhas leakage water using Lagrangian methods, finding  
105 considerably smaller transport estimates than previous Eulerian-based methods. Most recently,  
106 *Cetina-Heredia et al.* [2019] quantified the time that mesoscale eddies along the southeast coast of  
107 Australia retain water and pointed out the change in eddy shape relates to water exchange between  
108 the eddy interior and the background flow. Though Eulerian eddies can temporarily trap and  
109 transport water parcels and tracers (*Gaube et al.* [2015]; *Condie and Condie* [2016]), under the  
110 effects of stretching and filamentation, such eddies may lose coherence and experience leakage and  
111 deformation in the turbulent flow (*Haller* [2005]; *Early et al.* [2011]). The Lagrangian frameworks  
112 suggest that the coherent material transport is very limited in the ocean, and that Eulerian-based  
113 estimates of transport with strong assumptions about material coherence need revision. A systematic  
114 quantification of the Eulerian eddy leakiness over their full lifespan has, to our knowledge, not yet  
115 been attempted.

116 The main goal of this study is to answer the following key issues: (1) What are the differences  
 117 between Eulerian and Lagrangian eddies in terms of coherent transport? (2) How leaky are Eulerian  
 118 eddies over their lifetime? We choose rotationally coherent Lagrangian vortices (RCLVs) and sea  
 119 surface height (SSH) eddies as the representative of Lagrangian eddies and Eulerian eddies in this  
 120 study. The paper is organized as follows. In Section 2, we present a brief description of the idealized  
 121 eddy-resolving model and two different coherent eddy identification methods. In Section 3, we  
 122 compare general statistical features of Lagrangian eddies to those of Eulerian eddies. In Section 4,  
 123 we examine the material flux across SSH eddy boundaries. Section 5 describes the material flux for  
 124 random-circle eddy model, as a baseline for comparison against the SSH eddies. Discussion and  
 125 conclusions are shown in Section 6.

## 126 2 Methods

### 127 2.1 Description of idealized model

128 Our goal is to create an eddy-resolving simulation which produces materially coherent eddies  
 129 with characteristics and spatial variability broadly similar to those of the real ocean. Because a  
 130 past study focused on the Pacific basin *Abernathey and Haller* [2018], here we create an idealized  
 131 Pacific-like scenario. The Massachusetts Institute of Technology general circulation model (MITgcm;  
 132 *Marshall et al.* [1997a,b]) is employed to construct an eddy-resolving idealized model with a 0.1  
 133 degree resolution. This resolution is adopted by many state-of-the-art global climate models (e.g.  
 134 GFDL CM2.6) and it allows the model to resolve the deformation radius with least 2 grid points at  
 135 about 40° N. North of this latitude is must be considered eddy permitting (*Hallberg* [2013]). The  
 136 model domain (shown in Fig. 1d) is a rectangular basin spanning 144 degrees in longitude and 60  
 137 degrees in latitude. It is bounded by simple land masses along the western and eastern boundary,  
 138 closely approximating the topography of the North Pacific, which is motivated by the model of *Cox*  
 139 [1985]. A no-slip condition is imposed at four solid boundaries. The basin bottom is flat and 4000 m  
 140 deep, except for a continental shelf along the western boundary, obeying an exponential profile from  
 141 200 m at the land to 4000 m in 4 degrees to the east of the land. Vertically, there are 29 unevenly  
 142 spaced layers, ranging from 10 m at the surface to 500 m at the bottom.

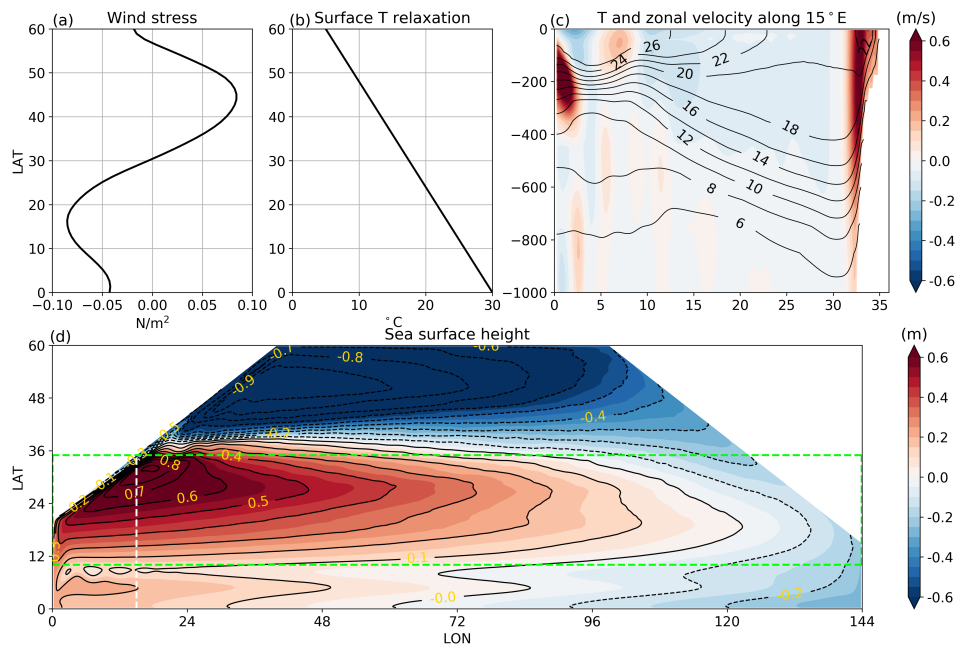
143 The surface forcing in the model consists of zonally uniform zonal wind stress and surface  
 144 temperature relaxation. The wind stress profile is based on zonally averaged zonal wind stress over  
 145 the North Pacific from QuikSCAT (*Risien and Chelton* [2008]). The surface temperature relaxation  
 146 forcing is described as a linear function of latitude only, with the value decrease from 30°C at the  
 147 equator to 5°C at 60° N. The relaxation time scale is 1 month. The distributions of wind stress  
 148 and surface temperature forcing are shown in Figure 1 (a) and (b). In order to maintain the vertical  
 149 stratification in the tropical region, we introduce a narrow sponge layer along the southern boundary,  
 150 in which the temperature is relaxed to prescribed stratification profile from World Ocean Atlas 2013  
 151 (<https://www.nodc.noaa.gov/OC5/woa13/woa-info.html>) with a time scale of one month. For the sake  
 152 of model simplicity, a linear equation of state is adopted and the salinity equation is turned off. The  
 153 nonlocal K-profile parametrization (KPP; *Large et al.* [1994]) is used to parameterize vertical mixing  
 154 in the surface boundary layer, and the Modified Leith Viscosity (*Fox-Kemper and Menemenlis* [2008])  
 155 is adopted for numerical viscosity. Full details about the physical and numerical parameters used in  
 156 the model and a reproducible configuration are available at [https://github.com/liutongya/Box\\_model](https://github.com/liutongya/Box_model).

157 The model run consists of three stages. In the first stage, a coarse grid model with a 1 degree  
 158 resolution is integrated for 300 years, whereupon a near steady state circulation is obtained indicated  
 159 by the mean kinetic energy. Then the 0.1 degree model is initialized at this point via interpolation and  
 160 integrated for 100 years to generate the circulation brimming with eddies. Finally, the Lagrangian  
 161 particle advection and eddy identification is conducted on the basis of the eddy-resolving solution  
 162 for another 5 years.

163 Climatological averages are calculated over the last 50 years and are used to assess this idealized  
 164 solution via comparisons with previous literature and observations of gyre structure, vertical strati-  
 165 fication, and eddy kinetic energy (EKE) distribution. As shown in Figure 1 (d), the uniform zonal

166 wind stress generates a double gyre circulation, with a strong concentrated eastward flow (like the  
 167 Kuroshio extension) between the subtropical and subpolar gyres. The pattern of sea surface height  
 168 (SSH) is quite comparable to mean dynamic topography derived from satellite and in situ data (see  
 169 Figure 3 in *Rio et al.* [2011]). The latitude-depth section of temperature along 15° E (approximately  
 170 equivalent to 137° E in real ocean) is shown in Figure 1 (c, black contours), together with zonal  
 171 velocity expressed by colors. The model captures the main features of thermal structures and banded  
 172 flows in tropical and subtropical regions reflected by hydrographic surveys in *Qiu and Chen* [2010]  
 173 (Figure 2). That is, the main thermocline (taking the 10° C isotherm) deepens strongly with latitude  
 174 in the subtropical interior, and then upraises suddenly at about 32° N. In addition, the comparison  
 175 of EKE distributions between AVISO data and model result indicates the model properly reproduces  
 176 two eddy bands in the subtropical circulation, with one band located in Kuroshio extension region  
 177 and another one located in the North Equatorial Current (NEC) region. A supplementary animation  
 178 of daily SST in the final year is available at <https://vimeo.com/341264533>.

179 Overall, the idealized model well simulates the general wind-driven circulation with strong  
 180 eddy activity in the upper ocean. This simulation is a computationally efficient way to probe eddy  
 181 dynamics at a resolution similar to contemporary state-of-the-art high-resolution global climate  
 182 models. Based on the results of *Sinha et al.* [2019], we expect that higher resolution would probably  
 183 lead to fewer coherent eddies, due to the emergence of submesoscale structures at mesoscale eddy  
 184 boundaries, but we do not pursue the question of resolution dependence here.



185 **Figure 1.** Model forcing fields and climatological results. (a) wind stress, (b) relaxation temperature, (c)  
 186 temperature (black contours) and zonal velocity (colors) profile along 15°E, and (d) sea surface height. The  
 187 white dashed line is the profile for (c). The green dashed line box is the region for eddy identification.

## 189 2.2 Identification of Lagrangian and Eulerian eddies

190 In the final 5 years, the Lagrangian particles are initialized with uniform spacing of  $1/80^{\circ}$  on  
 191 the surface covering the whole domain, with more than 55 million points. As described in *Haller*  
 192 *et al.* [2016] and *Abernathey and Haller* [2018], a dense mesh of Lagrangian particles, much higher  
 193 resolution than the model grid itself, is necessary to reflect the fine structure of transport barriers and  
 194 properly identify Lagrangian eddies. The particles can be advected for 90 days by 2D surface flow

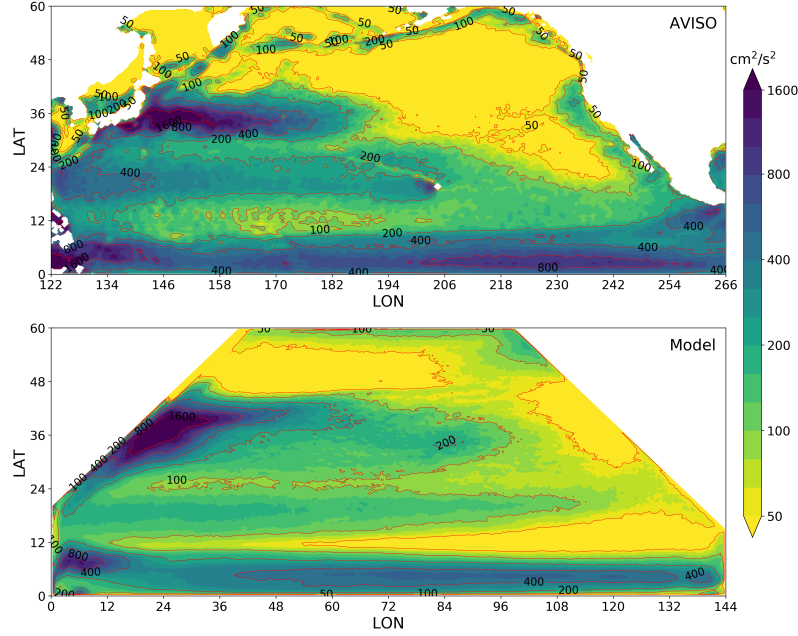


**Figure 2.** Comparison of EKE fields from (upper) AVISO and (bottom) model.

188

195 in "online mode" till the next initialization. In the following analysis, we use 20 non-overlapping  
 196 90-day time intervals in total for identifying eddies. In this paper our focus is on the near-surface  
 197 horizontal flow, and consequently our particles are advected by the surface flow only (top model  
 198 vertical level). Such trajectories are thus most representative of buoyant material such as marine  
 199 debris or pollutants. However, due to the relatively low Rossby number and consequently weak  
 200 divergence in the 2D flow, these trajectories are reasonably close to full 3D trajectories. (This was  
 201 confirmed by full 3D advection tests.) A future study in preparation will examine the 3D structure  
 202 of material eddies in this simulation.

203 Our definition of a Lagrangian eddy, one of many possible choices, is based on the concept  
 204 of coherent rotation. Over its lifetime, all water parcels along a coherent eddy boundary should  
 205 have the same average angular speed when rotating around the eddy core, in analogy to rigid-body  
 206 rotation,. Based on this physical concept, *Haller et al.* [2016] proposed that the material boundary  
 207 of a rotationally coherent Lagrangian vortex (RCLV, also called Lagrangian eddy) can be found by  
 208 identifying the outermost closed contours of the Lagrangian-averaged vorticity deviation (LAVD,  
 209 adopted by *Abernathey and Haller* [2018]; *Tarshish et al.* [2018]; *Sinha et al.* [2019]).

210 In a two dimensional flow, given a finite time interval  $(t_0, t_1)$ , LAVD is defined as the average of  
 211 the vorticity deviation along the Lagrangian particle trajectory, that is,

$$LAVD_{t_0}^{t_1}(x_0, y_0) = \frac{1}{t_1 - t_0} \int_{t_0}^{t_1} |\zeta'[X(x_0, y_0, t), Y(x_0, y_0, t), t]| dt. \quad (1)$$

212 Where  $(X, Y)$  denotes the position for the particle initially located in point  $(x_0, y_0)$  and  $\zeta'$  indicates  
 213 the instantaneous relative vorticity deviation from the spatial average over the whole domain. LAVD  
 214 reflects the average magnitude of local rotation for each Lagrangian particle over the time interval.  
 215 The Lagrangian view makes it essentially different from Eulerian detection methods, for instance,  
 216 defining coherent eddies by instantaneous vorticity contours. The local maximum of the LAVD field  
 217 (corresponding to the strongest local rotation) represents the Lagrangian vortex center, and the vortex  
 218 boundary is the outermost closed LAVD curve encircling the center.

219 Any closed curve of the LAVD field is a plausible, objective choice for the Lagrangian eddy  
 220 boundary. To constrain our choice of boundary, we employ two additional heuristics. Convexity  
 221 deficiency (CD), defined by *Haller et al.* [2016], describes how strongly the boundary curve departs  
 222 from a convex curve. Coherency index (CI), introduced by *Tarshish et al.* [2018], measures how  
 223 much the particles within the eddy disperse away from the eddy center over the time interval. Starting  
 224 from a local maximum of LAVD, we search outward for the closed LAVD contour using a bisection  
 225 search algorithm, until we obtain the outermost contour satisfying both CD and CI thresholds. The  
 226 sensitivity analysis in *Tarshish et al.* [2018] showed that CD choices of 0.01, 0.1, and 0.25 are  
 227 representative values for identifying strictly coherent, moderately coherent, and leaky vortices. In  
 228 this study, we choose  $CD=0.1$ , and  $CI=-2$  is adopted based on relationship between CI and CD (their  
 229 Figure 12). We have integrated the LAVD detection method into an open source Python package  
 230 named `floater` available at <https://github.com/rabernat/floater>.

231 The method we use to detect and track SSH eddies is described in *Faghmous et al.* [2015]. This  
 232 geometric eddy identification method is very similar to that proposed by *Chelton et al.* [2011] and  
 233 detects mesoscale eddies based on closed contours of SSH anomaly (SSHA) data. Similar to *Chelton*  
 234 *et al.* [2011], they published a global daily mesoscale ocean eddy map over a period of 1993-2004  
 235 from the AVISO dataset. However, *Faghmous et al.* [2015] developed an open source MATLAB  
 236 code which can be applied to reproduce their detection algorithm and apply it to new scenarios.  
 237 The algorithm is available at <https://github.com/jfaghm/OceanEddies>. We used this code to detect  
 238 Eulerian eddies in our model.

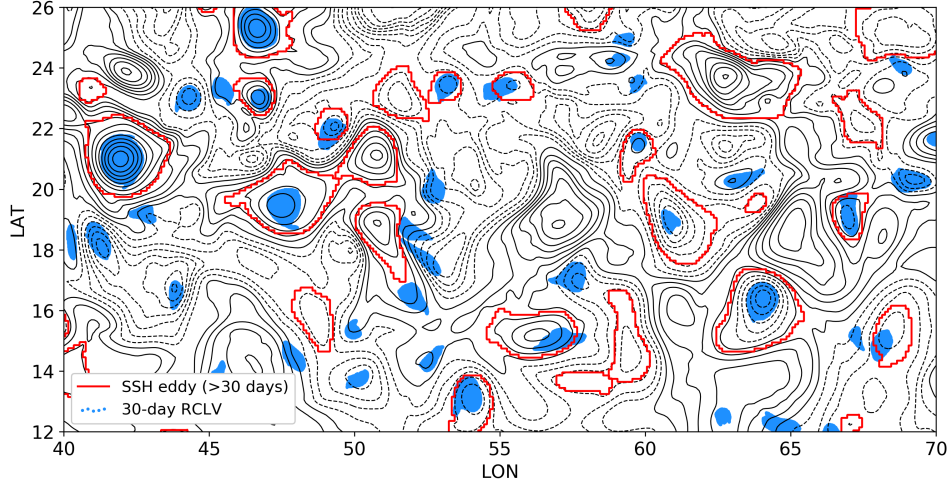
### 239 **3 Census of Lagrangian vortices and Eulerian eddies**

#### 240 **3.1 Quantity statistics of eddies**

241 In the subtropical region (green dashed line box shown in Figure 1d), the LAVD method and  
 242 SSH contour method are applied to identify RCLVs and SSH eddies in 20 90-day time intervals.  
 243 Compared to SSH eddies, the most peculiar thing about RCLVs is that they are identified on specific  
 244 time intervals. In this case, we initialize the detection at the first day of each 90-day time interval and  
 245 then identify 30-, and 90-day RCLVs from that initialization date. For SSH eddies, the identification  
 246 is carried out continuously in 5 years and the complete SSH eddy dataset is obtained. To compare  
 247 RCLVs and SSH eddies in the same time interval, we extract SSH eddies from the complete dataset,  
 248 by the condition that the SSH eddy has existed on the RCLV initialization time and can last for more  
 249 than 30 and 90 days from that date. The model resolution (about 10 km) is insufficient to resolve  
 250 submesoscale structures, so the eddies with the radius less than 25 km are excluded.

251 In Figure 3, we randomly choose a small region ( $40^{\circ}$ - $70^{\circ}$  E &  $12^{\circ}$ - $26^{\circ}$  N) to show the initial  
 252 locations of detected 30-day RCLVs and SSH eddies with lifespans longer than 30 days, with the  
 253 SSHA field superimposed. Based on whether there is a RCLV whose center is located within the  
 254 boundary of a SSH eddy, all eddies can be classified into three categories: overlapping RCLVs and  
 255 SSH eddies, non-overlapping SSH eddies, and non-overlapping RCLVs. For overlapping RCLVs  
 256 and SSH eddies, one notable character is that the RCLVs have a much smaller area than that of the  
 257 corresponding SSH eddy and are enclosed by SSHA contours, which is consistent with the results  
 258 of *Abernathy and Haller* [2018]. For non-overlapping SSH eddies, though they are identified and  
 259 tracked by Eulerian detection algorithm, they do not maintain material coherence over the detection  
 260 time interval. For example, an Eulerian eddy with with a large SSHA amplitude (such as the one  
 261 located in about  $63^{\circ}$  E &  $24^{\circ}$  N) appears to be a eddy, but our result in section 4 illustrate that this  
 262 kind of eddy may not be a materially coherent structure. Conversely, the non-overlapping RCLVs  
 263 are the Lagrangian structures that SSH contour algorithm fails to identify. Among non-overlapping  
 264 RCLVs, there are a fraction of vortices (about 25% of total RCLVs) that are not located nearby the  
 265 local peak of SSHA. They are quite different from the classic geostrophic eddy centered on an SSHA  
 266 extremum, but they are indeed materially coherent as indicated by LAVD method. Here we mainly  
 267 focus on examining the leakiness of SSH eddies, so we will not discuss the details of these special  
 268 RCLVs in this paper. The statistics presented below confirm that these results are typical rather than  
 269 anomalous.





270 **Figure 3.** The initial locations of 30-day RCLVs and SSH eddies (>30 days) in a randomly selected time  
 271 interval and region. The blue dots present particles within each RCLV boundary. The red lines denote SSH  
 272 eddy boundaries. The SSHA contours are shown in black solid and dashed lines, with the contour interval of 1  
 273 cm.

274 The statistics for the total numbers of RCLVs and SSH eddies are shown in Figure 4. We  
 275 identify 5412 RCLVs and 4144 SSH eddies (extracted from the complete dataset) with lifetimes  $\geq 30$   
 276 days in subtropical region over five years. The numbers of 30-day RCLVs in each 90-day interval  
 277 fluctuates between 250 and 300. The longer-lived vortices are rare, with about 70 in each interval for  
 278 90-day RCLVs. A similar ratio of >90 days eddies to >30 day eddies (1/5) is found in SSH eddies.  
 279 Another interesting observation is that the total number of SSH eddies is slightly less than that of  
 280 RCLVs, since non-overlapping RCLVs are the most numerous type. The >30 days overlapping SSH  
 281 eddies only account for 47.6% of the total, which means about half of SSH eddies (>30 days) have  
 282 no coherent core inside.

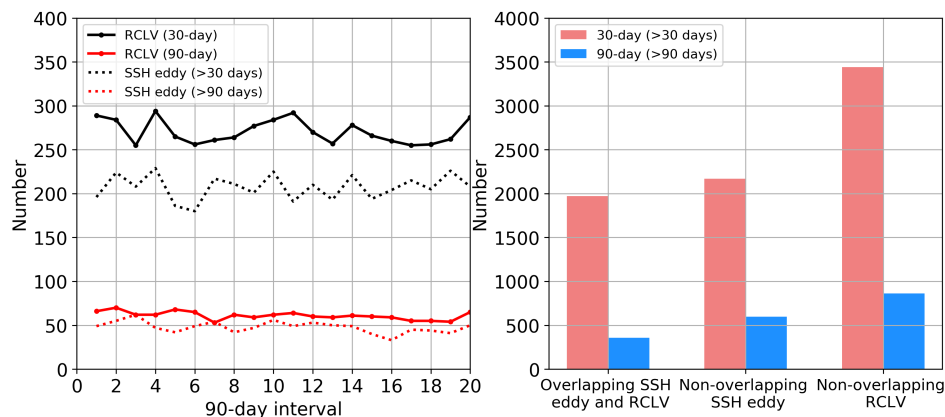
### 288 3.2 Radius, propagation speed, and zonal coherent transport

289 The equivalent radius  $R$  of RCLVs and SSH eddies is converted from the eddy horizontal area  
 290  $A$  by the formula  $R = \sqrt{A/\pi}$ . We also calculate the first Rossby radius of deformation  $L_d$  via

$$L_d = \frac{1}{f\pi} \int_{-H}^0 N(z) dz, \quad (2)$$

291 where,  $f$  is the Coriolis parameter for earth rotation and latitude,  $H$  is the water depth, and  $N(z)$  is  
 292 the buoyancy frequency obtained from model vertical stratification.

293 The top two panels in Figure 5 show the comparison of radius for 30-day RCLVs and SSH  
 294 eddies with lifetimes longer than 30 days. A box-and-whisker plot represents statistics of all eddies  
 295 in  $2.5^\circ$  latitude bins. With the increase of Coriolis parameter, the first Rossby deformation radius  
 296 (purple dashed lines) decreases from about 95 km at  $10^\circ$  N to about 25 km at  $35^\circ$  N, which is  
 297 similar to the distribution in *Chelton et al.* [1998]. Comparing with SSH eddies, the mean RCLV  
 298 radius (35.5 km) is approximately about half of the mean SSH eddy radius (72.4 km). Similar to  
 299 this result, *Cetina-Heredia et al.* [2019] showed that the solid body rotation radius is 0.6 and 0.5 the  
 300 radius of anticyclonic and cyclonic eddies detected from velocity fields, respectively. In contrast with  
 301 *Abernathey and Haller* [2018], no significant latitude dependence or relationship with deformation  
 302 radius is visible in either RCLVs or SSH eddies. The SSH eddy radii of about 60 km in the low



283 **Figure 4.** RCLVs and SSH eddies number statistics. (left) Time series of RCLVs and SSH eddies number  
 284 in 20 90-day intervals. (right) Total numbers of overlapping SSH eddies and RCLVs, non-overlapping SSH  
 285 eddies, and non-overlapping RCLVs. The colors correspond to the eddy lifespans in both two panels. The ratio  
 286 of 30-day overlapping RCLVs (>30 days SSH eddies) to all 30-day RCLVs (>30 days SSH eddies) is 36.5%  
 287 (47.6%), and the ratio for 90-day (>90 days) eddies is 29.4% (37.5%).

303 latitudes (about  $10^\circ$  N) are smaller than the observation (more than 100 km). The relative lower  
 304 eddy activity in the region around  $10^\circ$  N (Figure 2) indicates our model may fail to generate realistic  
 305 eddies in the tropics, likely caused by biases in the model background state. Most of our focus in  
 306 what follows is on the midlatitudes.

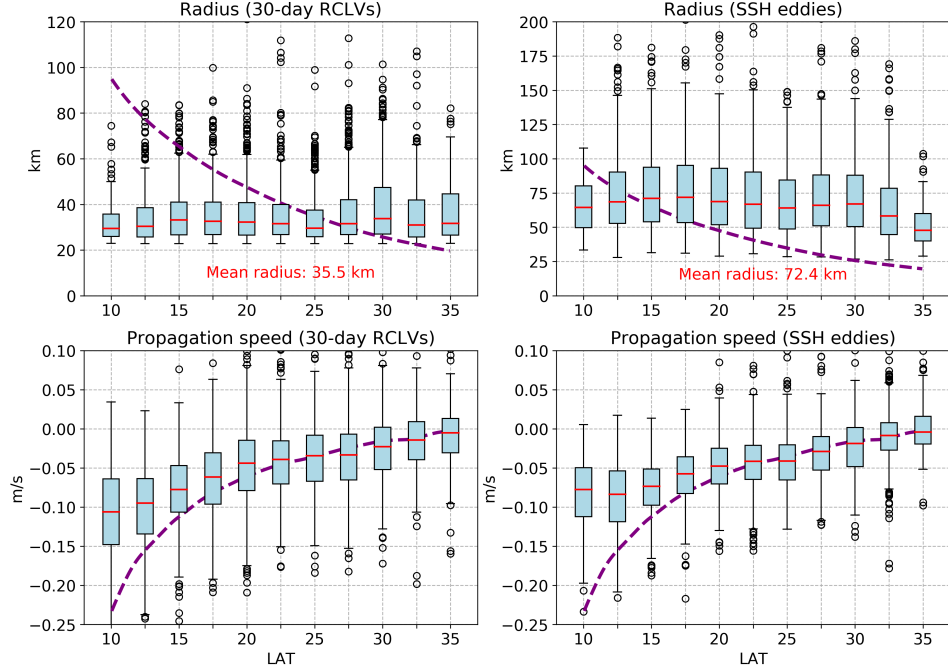
307 The zonal propagation speed  $c$  of RCLVs and SSH eddies, derived from the zonal displacement  
 308 over the lifetime, is shown in the bottom two panels of Figure 5. We observe RCLVs and SSH eddies  
 309 have similar westward propagation speeds at each latitude in the subtropical region, nearly consistent  
 310 with the phase speed of nondispersive long-wave Rossby wave (also captured by the result based on  
 311 AVISO data in *Abernathey and Haller* [2018]) except for the low latitude region. The phase speed  
 312  $c_p$  is calculated by

$$c_p = \bar{U} - \beta L_d^2, \quad (3)$$

313 where,  $\bar{U}$  is the depth-averaged zonal flow (*Kloeker and Marshall* [2014]).

320 Having obtained radius and zonal propagation speed of eddies, we now can estimate the advective  
 321 material transport by coherent eddy movement following the methods proposed by *Dong et al.* [2014]  
 322 and *Zhang et al.* [2014] These methods assume Eulerian eddy is materially coherent, trapping its  
 323 interior water parcels and translating them uniformly without water exchange with the surrounding  
 324 environment. (This is true by construction for RCLVs.) Here we temporarily assume SSH eddies are  
 325 materially coherent in order to make this calculation, despite evidence to the contrary. The vertical  
 326 depth and structure of coherent eddies is still an open issue; therefore, to avoid artificially introducing  
 327 the depth of eddies, we define cross-longitude transport by  $Q = cL_{yz} = 2Rc$ , with units of  $m^2/s$ .  
 328  $L_{yz}$  means the width of coherent eddy and  $Q$  depicts zonal transport on the surface induced by the  
 329 individual eddy. Figure 6 shows the zonally averaged zonal transport per degree latitude averaged  
 330 over 5 years for 30- and 90-day eddies. The coherent transport of RCLVs is uniformly smaller than  
 331 that of SSH eddies at each latitude, since the coherent core of RCLVs is only half of SSH eddy radius,  
 332 applying to both 30- and 90-day eddies. If the constant vertical depth 500 m is used to compute  
 333 volume transport, the peak value of the zonal advective transport for 30-day RCLVs is about 0.3 Sv,  
 334 much weaker than the estimate larger than 1 Sv in the Pacific ocean by *Zhang et al.* [2014] (see their  
 335 Figure 3).

336 These statistical results suggest that, the RCLVs and SSH eddies move at the similar speed, and  
 337 the zonal coherent transport by RCLVs is around half of the transport by SSH eddies due to large



314 **Figure 5.** (top) Radius and (bottom) propagation speed statistics of (left) 30-day RCLVs and (right) >30 days  
 315 SSH eddies. A box-and-whisker plot shows statistics of all eddies in 2.5 bins. The red line represents the  
 316 median. The blue box covers 25th-75th percentiles of the distribution. The black whiskers indicate 5th-95th  
 317 percentiles. The black circle symbols represent the outliers beyond 5th-95th percentiles. The purple dashed  
 318 line in top two panels is zonally averaged first baroclinic Rossby radius of deformation in kilometers. Mean  
 319 radii of RCLVs and SSH eddies (labeled in red text) are 35.5 km and 72.4 km, respectively.

338 coherent core defined by SSH contours. However, this is not the case; the next section shows that  
 339 the SSH eddies are far from materially coherent structures.

#### 342 4 Material Flux Across Eddy Boundaries

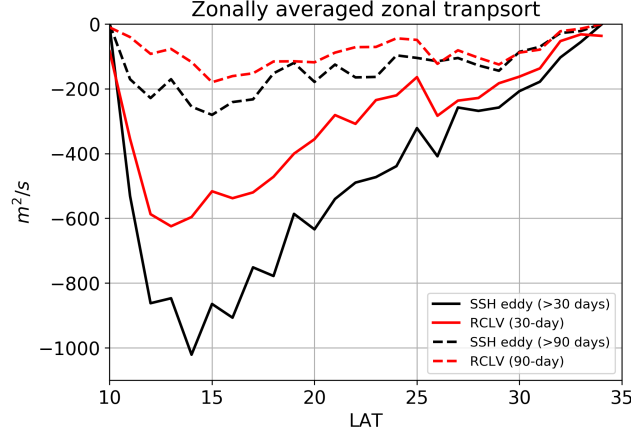
343 The RCLVs are materially coherent by construction, but the material coherence properties of  
 344 the SSH eddies require investigation. Having described the statistics of Lagrangian vortices and  
 345 Eulerian eddies, we now focus on the core issue of our study: how leaky are the Eulerian eddies in  
 346 terms of material transport?

##### 347 4.1 Reynolds transport theorem

348 For a conserved scalar  $\phi$  (e.g. conservative temperature for heat transfer) without source and  
 349 sink in a Boussinesq flow, the conservation equation is given by,

$$\frac{\partial \phi}{\partial t} + \vec{u} \cdot \nabla \phi = 0. \quad (4)$$

350 Here,  $\vec{u}$  is the velocity vector field. Consider a 2-D mesoscale eddy system and a coinciding control  
 351 surface  $\Omega$  with a control boundary  $\partial\Omega$ , according to Reynolds transport theorem (*Reynolds et al.*  
 352 [1903]), the time derivative of integrated  $\phi$  over the eddy system is determined by the time rate of  
 353 change of  $\phi$  within the control eddy surface and the net rate of flux of  $\phi$  through the moving eddy  
 354 boundary,



340 **Figure 6.** Zonally averaged zonal transport of RCLVs and SSH eddies (assuming SSH eddies could keep  
341 coherence).

$$\frac{d}{dt} \int_{\Omega} \phi dA = \int_{\Omega} \frac{\partial \phi}{\partial t} dA + \oint_{\partial \Omega} \phi \vec{u}_b \cdot \hat{n} dS. \quad (5)$$

355 Where,  $dA$  and  $dS$  are area and line elements,  $u_b$  is the velocity of eddy boundary, and  $\hat{n}$  is the  
356 outward-pointing unit normal vector. The definition of a material region is that the boundary  
357 velocity  $\vec{u}_b$  equals the fluid velocity  $\vec{u}$ . Combining Gauss's theorem and (3), (4) Reynold's transport  
358 theorem for a material eddy becomes

$$\frac{d}{dt} \int_{\Omega} \phi dA = \int_{\Omega} \frac{\partial \phi}{\partial t} dA + \oint_{\partial \Omega} \phi \vec{u} \cdot \hat{n} dS = \int_{\Omega} \left( \frac{\partial \phi}{\partial t} + \vec{u} \cdot \nabla \phi \right) dA = 0. \quad (6)$$

359 In words, when the eddy boundary is a material boundary, the total amount of  $\phi$  substance within  
360 the eddy is conserved, allowing the eddy to trap and translate its contents over large distances.

361 Generally, the velocity of Eulerian eddy boundaries (e.g. SSH contours in *Chelton et al.* [2011],  
362 PV contours in *Zhang et al.* [2014], and contours of the stream function field in *Nencioli et al.*  
363 [2010]) does not coincide with the fluid velocity because of the non-material detection method,  
364 which indicate the non-zero material flux across these boundaries. The question we address below  
365 is, *how much material leaks across the Eulerian eddy boundaries?*

## 366 4.2 Overlapping RCLVs and SSH eddies

367 The material flux across the eddy boundary can be understood as two processes: leakage and  
368 intrusion. Leakage means the initially inside water parcels escape into the background environment  
369 through the eddy boundary, and intrusion stands for the background water parcels entering into the  
370 eddy interior. Due to the practical difficulty of obtaining the eddy boundary velocity normal vector  
371 and conducting the integration along the curved boundary, we do not diagnose the material flux  
372 across the eddy boundary directly by (5). As a substitute, we approximate it via quantifying the  
373 number of Lagrangian moving across the eddy boundary. To do this, we employ the same Lagrangian  
374 particle experiments that were used to identify the RCLVs, described in the previous section.

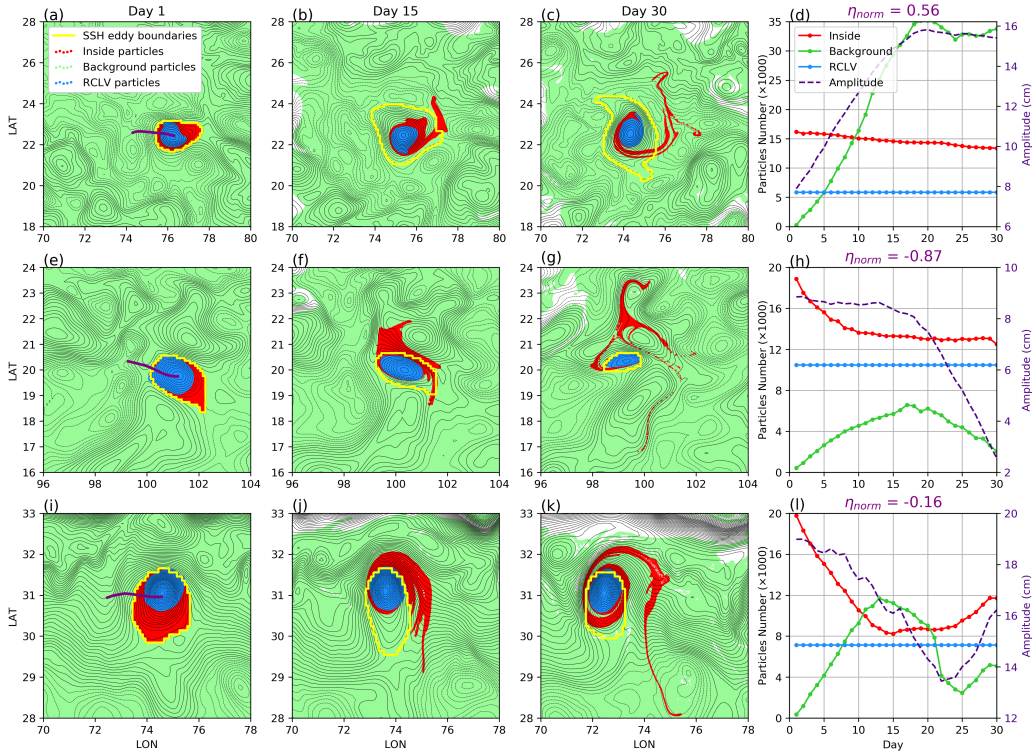
375 In this section we consider the leakage across Eulerian eddies which overlap with RCLVs,  
376 1973 eddies in total. For each eddy, the numbers of initially inside particles  $N_{in}(t)$  and background  
377 particles  $N_{out}(t)$  surrounded by SSH contour boundaries are calculated every day during the eddy  
378 lifetime. Specifically,  $N_{in}^0$  has the maximum value and  $N_{out}^0$  is 0. In addition, a normalized parameter

describing the change of amplitude at the eddy center point is defined by,  $d\eta_{norm} = (\eta_1 - \eta_0)/\overline{\eta(t)}$ , where  $\eta_0$ ,  $\eta_1$ , and  $\overline{\eta(t)}$  represent initial, final, and mean amplitude over the eddy lifetime, respectively. Base on the  $d\eta_{norm}$ , these eddies are classified into three categories: growing eddy ( $d\eta_{norm} > 0.25$ ), steady eddy ( $-0.25 \leq d\eta_{norm} \leq 0.25$ ), and decaying eddy ( $d\eta_{norm} < -0.25$ ). Each category accounts for about 30% of the overall sample, and the numbers are labeled in the legend of Figure 8.

Figure 7 depicts the processes of leakage and intrusion for three pairs of 30-day overlapping RCLVs and SSH eddies selected randomly, including the movement of particles and time series of particle numbers. The red dots represent the initial particles inside SSH eddy boundaries (inside particles). The green dots represent the initial particles outside SSH eddy boundaries (background particles). The blue dots indicate RCLVs particles. The trends of the amplitudes at the center points (purple lines) indicate they belong to growing eddy, decaying eddy, and steady eddy, respectively. These three SSH eddies all move westward and contain a coherent core (RCLV) trapping initial water inside its boundary in 30 days. Unlike the coherent transport by RCLVs, part of the initial water inside the SSH eddies rapidly escapes from the eddy interior and joins in the background environment, then moves along with the local current. Simultaneously, the background water can intrude into SSH eddies. Among these three cases, the leakage ratio of the initial water reach about 20%, 33%, and 40% at the end of the 30 days, respectively. The strongest intrusion occurs in the growing eddy, with about 34,000 Lagrangian particles from background flow intruding into it. This is because the eddy is expanding and more and more background water becomes enclosed by the outermost closed SSH contour. In contrast, the intrusion in the decaying eddy is relatively weak. To measure the rate of leakage and intrusion, the crossover point of leakage and intrusion trends is considered. The appearance of the crossover day means the volume of intruded water exceeds that of initial eddy water retained inside the SSH eddy. A quick (slow) crossover day corresponds to a strong (weak) material flux across boundaries. In this example, for both the growing and steady eddy, the crossover day is about 10th day. The decaying eddy, in contrast, has no crossover day because the intrusion is weak, due to the continuously decreasing eddy volume. Besides the coherent RCLV core, there appear to be some initial particles enclosed by SSH eddy boundaries, but not recognized as part of the Lagrangian coherent structure. The LAVD algorithm does not include this structure as part of RCLV, because it rotates differently from the main coherent core, existing in the form of filaments. A supplementary animation to show these three leaky SSH eddies is available at <https://vimeo.com/341157321>.

This material flux across SSH eddy boundaries from these random cases illustrates that the water surrounded by SSH contours at neighboring time is not necessarily the same fluid. Since leaky part does not contribute to the coherent transport, the transport estimate based on SSH eddy boundaries may strongly overestimate the real coherent material transport, as represented by the RCLV core.

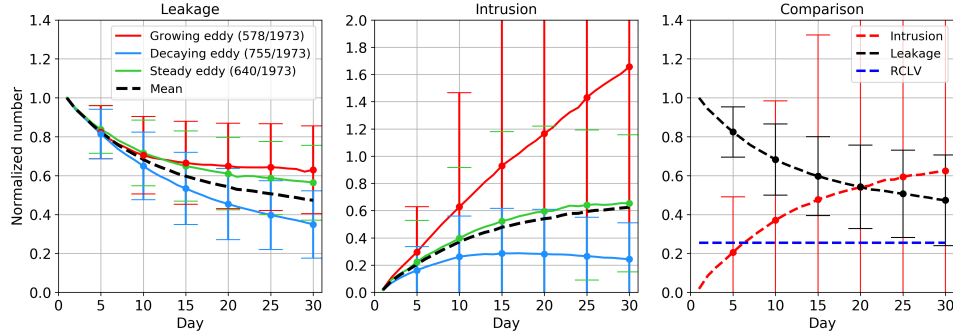
In the following statistical analysis, the leakage and intrusion processes are normalized by the initial particle numbers inside SSH eddy boundaries (equivalent to the initial eddy size), which are given by  $\frac{N_{in}(t)}{N_{in}^0}$  and  $\frac{N_{out}(t)}{N_{in}^0}$ , and their mean trends across all eddies are described as  $\frac{\overline{N_{in}(t)}}{N_{in}^0}$  and  $\frac{\overline{N_{out}(t)}}{N_{in}^0}$ . Figure 8 shows the normalized leakage trend and intrusion trend for all 30-day overlapping SSH eddies. The leakage ratio equals to 1 minus the normalized number of the leakage trend (amount of initially inside particles still retain inside SSH eddy interior). And the intrusion ratio, the normalized number of the intrusion trend, increases from 0 with the background particles intruding into the SSH eddy. The mean leakage ratio of all eddies is about 50%, which indicates roughly half of water initially enclosed by the SSH contour is not coherently carried by the moving SSH eddy by the end of the detection period. The degree of leakage and intrusion for different categories of eddies are distinctive. Growing eddies and decaying eddies corresponds to weaker (40%) and stronger (60%) leakage of initial water, respectively. And the contrary trait is observed in the process of intrusion. The large mean value and standard deviation (red line and error bars in middle panel) for intrusion trend is from the growing eddy, whose normalized intruded particle number may be very large if the eddy area expands for several times than initial size. For steady eddies, the behavior of the leakage curve is close to that of growing eddies, with the leaky water accounting for about 40%. Besides the



415 **Figure 7.** (the first three columns) The particle locations around three randomly selected overlapping eddies  
 416 over 30 days. (the fourth column) Time series of particle numbers for these three eddies. The growing eddy,  
 417 the decaying eddy, and the steady eddy is shown in (a-d), (e-h), and (i-l), respectively. The red dots represent  
 418 the initial particles inside SSH eddy boundaries (inside particles). The green dots represent the initial particles  
 419 outside SSH eddy boundaries (background particles). The blue dots indicate RCLVs particles. The yellow lines  
 420 are SSH eddy boundaries. The center points trajectories of SSH eddies are superimposed in purple lines. The  
 421 normalized amplitude change of three eddies are labeled in (d, h, and l).

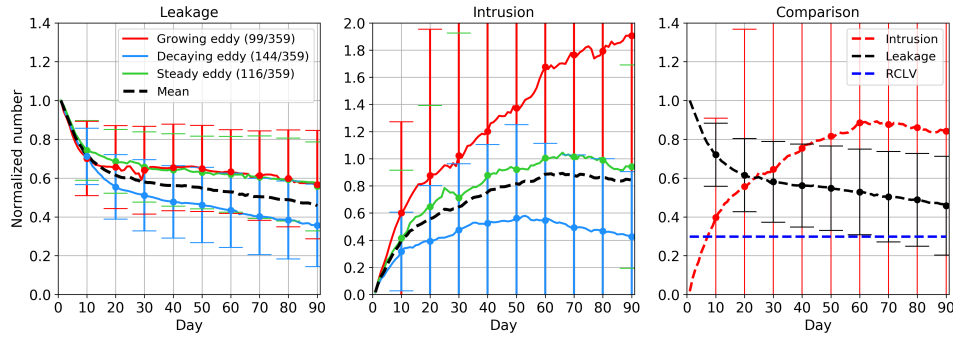
438 leaky part, the truly coherent structure (RCLV) accounts for about 25% of initially inside water, and  
 439 its material boundary ensure the volume of this part of water remains constant during the lifetime  
 440 (see dashed blue line in the right panel). The additional 25% or retained water evolves as a filament  
 441 structure but still remain inside the SSH eddy boundary. The crossover time of averaged leakage and  
 442 intrusion is 20 days.

443 We also estimate the material flux for the 359 longer-lived 90-day eddies. The results, shown  
 444 in Figure 9, display similar behaviors to those of 30-day eddies, including the trends of leakage and  
 445 intrusion for three categories of eddies. The average leakage ratio at the final time is about 50%  
 446 as well. The crossover day of leakage and intrusion occurs on about 23th day. After the crossover  
 447 day, the rate of leakage and intrusion become obviously slow, because mostly only the coherent core  
 448 remains. Figure 10 shows histograms of the crossover day for 30- and 90-day SSH eddies. Grouped  
 449 by eddy growth stage, for both shorter-lived and longer-lived eddies, the crossover day occurs in the  
 450 sequence growing eddies, steady eddies, and decaying eddies. About 50% decaying 30-day eddies  
 451 have no crossover day due to the weak intrusion. Distinct features are not observed when we group  
 452 eddies as cyclonic and anticyclonic (not shown).



453 **Figure 8.** (left) Normalized leakage trend, (middle) intrusion trend, and (right) the comparison of leakage  
 454 and intrusion for 30-day overlapping SSH eddies. The numbers of three categories of eddies are labeled in the  
 455 legend in the left panel. The error bar indicates one standard deviation of the mean over all samples on that day.  
 456 The normalized number of the leakage trend (decreasing from 1) shows the amount of initially inside particles  
 457 still retain inside SSH eddy interior. The normalized number of the intrusion trend (increasing from 0) stands  
 458 for the amount of background particles intrude into the SSH eddy.

The invariable blue dashed line in the right panel indicates normalized RCLV particle number.



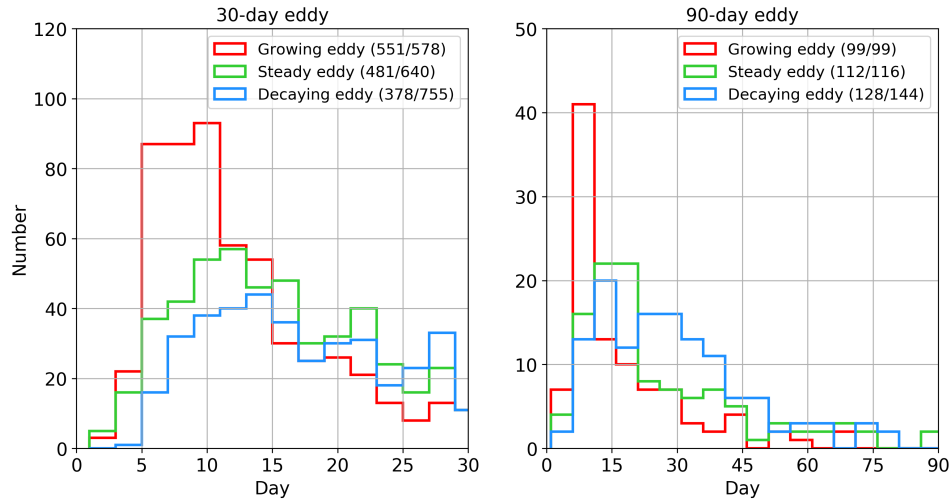
459 **Figure 9.** Same as Figure 8, but for 90-day overlapping eddies.

### 463 4.3 Non-overlapping SSH eddies

464 The above examples give the impression that SSH eddies contain a coherent material core;  
 465 however, we have so far only examined overlapping SSH and RCLV eddies. We now turn to the  
 466 numerous non-overlapping SSH eddies, which account for roughly half of SSH eddy samples.

467 These SSH eddies can be detected by the SSHA contour method, but there is no Lagrangian  
 468 coherent structure inside these SSH eddies. Thus we anticipate stronger exchange with the back-  
 469 ground. Figure 11 shows the movement of particles in 30 days around three randomly selected  
 470 non-overlapping SSH eddies. For the growing eddy (top panels), after 30 days the SSH eddy is  
 471 almost filled with intruded water, along with more than 90% initial water leaking out the boundary.  
 472 Some particles still remain in the eddy interior for decaying eddy (middle panels) and steady eddy  
 473 (bottom panels), but evidently these do not meet the requisite criteria for RCLV detection. The  
 474 statistical results are shown in Figure 12. On average, the leakage for non-overlapping eddies reaches  
 475 60%, stronger than that of overlapping SSH eddies with a coherent core. In the same way, the intru-  
 476 sion process is also stronger compared to overlapping SSH eddies. And we note that the crossover  
 477 day of leakage and intrusion is the 12th day, revealing that the material flux occurs at a faster rate.

478 Tightening the contour threshold will not enable non-overlapping SSH eddies keep the material  
 479 coherence properties because of the strong leakage and intrusion process, which suggests that the



460 **Figure 10.** Histograms of the crossover day for (left) 30-day and (right) 90-day SSH eddies. Growing eddies,  
 461 steady eddies, and decaying eddies are indicated by red, green, and blue lines, respectively. The number of  
 462 eddies with the crossover day and the total number in each group are labeled in the legends.

480 eddy coherence properties depend on whether the organization method is material, rather than the  
 481 choice of thresholds or parameters. In other words, the water exchange across SSH eddy boundaries  
 482 over the eddy whole lifetime shows the SSH eddies are far from materially coherent structures.

## 496 5 Random-Circle Eddy Model

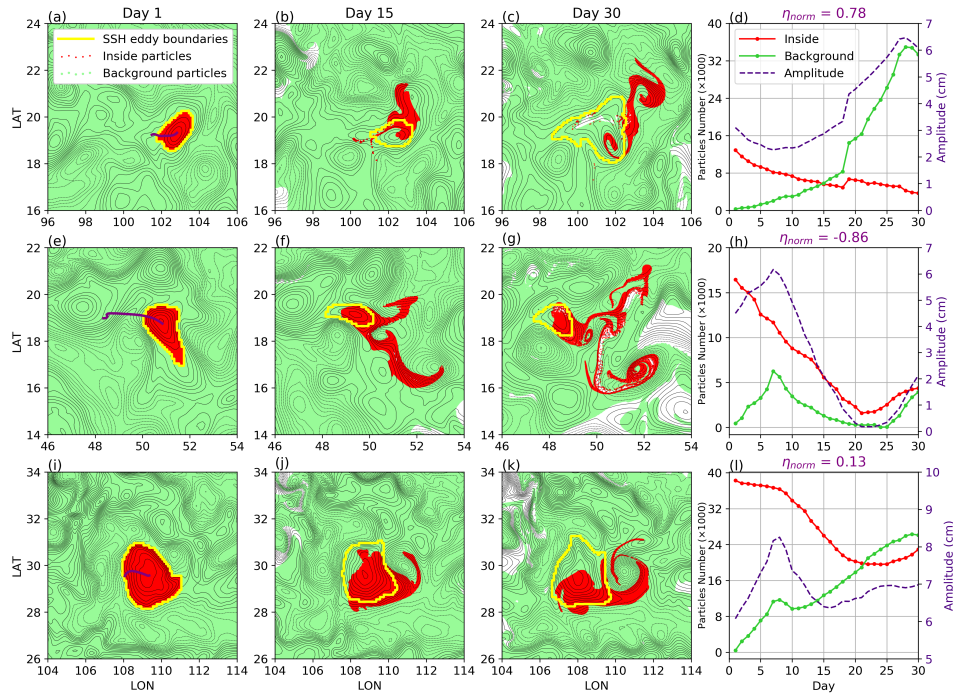
497 The analysis above showed that the non-overlapping SSH eddies were significantly leakier than  
 498 the ones that overlapped with RCLVs. But is there still some inherent material coherence to these  
 499 SSH eddies that the RCLV detection algorithm fails to identify? In this section, we calculate the  
 500 degree of leakage and intrusion around completely artificial eddies defined by randomly generated  
 501 circles. This allows us to assess the differences in the material coherence properties between SSH  
 502 eddies and arbitrary patches of water.

503 For a fair comparison, we generate a dataset of artificial eddies based on the statistical features  
 504 of SSH eddies. The number distribution with radius of overlapping SSH eddies is displayed in Figure  
 505 13 (left), which suggests that more than 70% of overlapping SSH eddies range from about 50 km to  
 506 90 km in radius. Here, the SSH eddies with radius larger than 170 km are excluded because of their  
 507 infrequent occurrence. Following this number and radius distribution, we structure the same amount  
 508 of circles in the subtropical region for the following random eddy experiments. The initial locations  
 509 of these circles are randomly selected in the subtropical basin during a random 90-day time interval.  
 510 The random choice of the initial position and occurrence time distributes these 1969 circles roughly  
 511 uniformly over the study region and time interval.

512 We set up two simple scenarios for the random-circle eddy model. In scenario 1, the positions  
 513 of the artificial circles are fixed at their initial positions. In scenario 2, these circles are advected by  
 514 the mean velocity of the center point over 30 days. The radius of the random-circle remains constant  
 515 for both two cases in the experiment, without the growth or decay of size. A quantification of leakage  
 516 and intrusion across boundaries is conducted for the fixed-circle model and moving-circle model.

517 Figure 14 shows the process of material flux across artificial boundaries for two randomly  
 518 selected circles from two different scenarios. For the fixed circle (top panels), which is initially  
 519 overlaid on several closed SSH contours, the initial water parcels inside the circle boundary leak  
 520 into the background flow in a fast rate, with the particle number decreasing above 80%, from about





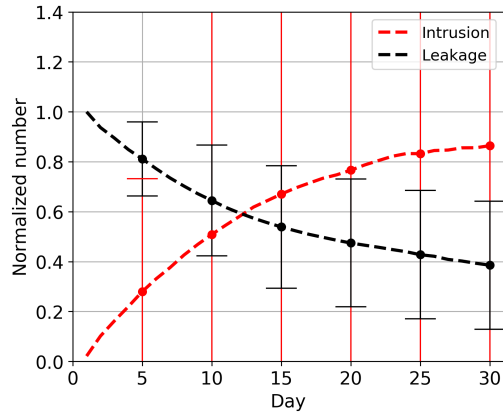
483 **Figure 11.** Same as Figure 7, but for three randomly selected non-overlapping SSH eddies. The top, middle,  
 484 and bottom panels correspond to a growing eddy, a decaying eddy, and a steady eddy, respectively.

521 19000 to about 3000 in 30 days. Figure 14 (a-c) shows that some initial particles surrounded by the  
 522 boundary on the 30th day do not always remain inside the circle, but rather reenter into the circle  
 523 carried by an eddy-like structure after a quick leakage. For the moving circle (bottom panels), which  
 524 propagates westward following the mean flow, about 30% initial particles remain after 30 days. The  
 525 crossover time is 12 days, which indicate the leakage rate is slower comparing with the fixed case (7  
 526 days). These two cases suggest that, even though there is no the coherent structure, initial particles  
 527 defined by artificial boundaries still have the possibility to remain inside these boundaries under  
 528 effects of local background flow field.

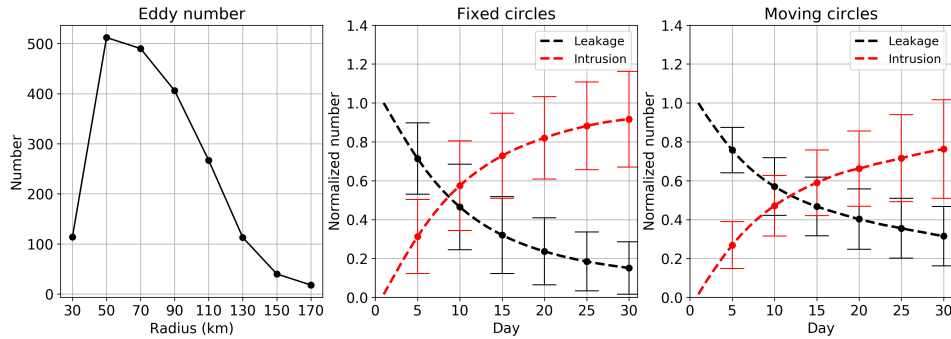
529 Statistical results of normalized leakage and intrusion from fixed circles model and moving  
 530 circles model are shown in Figure 13 (right two panels). After 30 days, there are about 18% and  
 531 32% initial water surrounded by these artificial boundaries for fixed and moving cases, respectively.  
 532 The standard deviation of the intrusion for random-circles is close to that of the leakage, in contrast  
 533 to the real SSH eddies. The reason is that the size of the random circle is constant, so there is no  
 534 large normalization value of intrusion which is common in real eddies accompanying with the eddy  
 535 size expansion. In particular, the leakage and intrusion trends of moving circles are quite similar to  
 536 those of non-overlapping SSH eddies, and their crossover times are both 12 days.

537 Figure 15 displays the bar diagram for the ratio of leakage and intrusion after 30 days from  
 538 5 categories of eddies (circles), including RCLVs, overlapping SSH eddies, non-overlapping SSH  
 539 eddies, fixed circles, and moving circles. RCLVs by construction have no leakage and intrusion  
 540 during the lifetime because their boundaries are material. Among the other 4 cases, the leakage in  
 541 30 days for SSH eddies with the coherent core (overlapping SSH eddies) is the weakest, but it still  
 542 exceeds 50% of initial water parcels.

543 These findings suggest that, though there is a slight difference in the magnitude of leakage and  
 544 intrusion ratio, the material coherence properties of non-overlapping SSH eddies (about half of SSH



485 **Figure 12.** The averaged leakage and intrusion trend for non-overlapping SSH eddies in 30 days. The error  
 486 bar indicates one standard deviation of the average over all eddies on the same day.



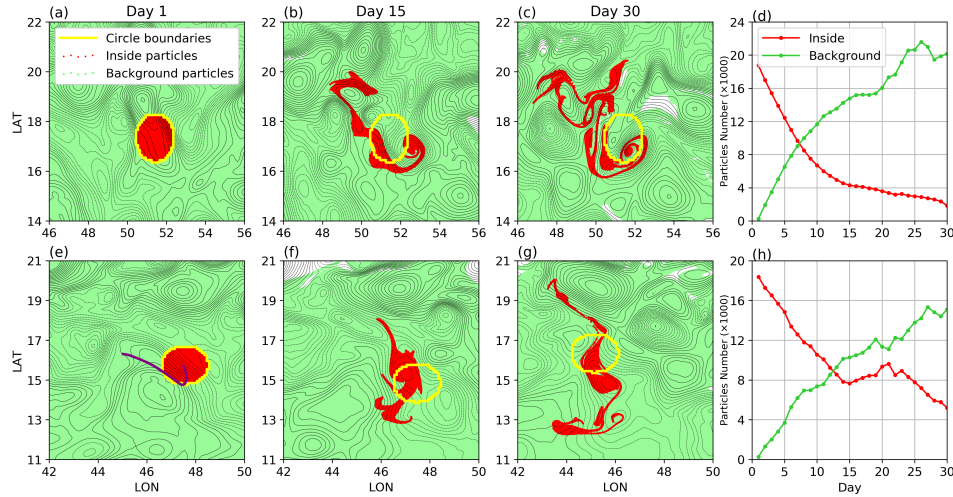
487 **Figure 13.** (left) The SSH eddy number distribution with radius. (middle and right) The averaged leakage  
 488 and intrusion trend for randomly selected fixed and moving circles in 30 days. The error bar indicates one  
 489 standard deviation of the average over all circles on the same day.

545 eddy samples) are not significantly different from randomly selected pieces of ocean with the same  
 546 size.

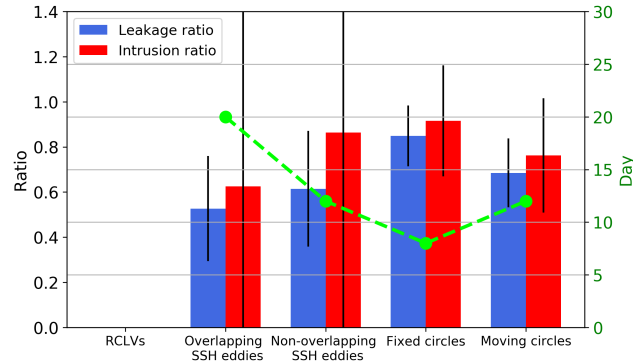
## 547 6 Discussion and Conclusions

548 Existing coherent eddy identification methods can be classified into two general categories:  
 549 Eulerian (e.g., *Chelton et al. [2011]*, *Nencioli et al. [2010]*, *Faghmous et al. [2015]*) and Lagrangian  
 550 (e.g., *Beron-Vera et al. [2013]*, *Haller et al. [2016]*). A wealth of literature has reported some  
 551 provocative results about coherent eddy transport based on Eulerian eddy boundaries, especially  
 552 the surprising zonal eddy mass transport (30Sv) in *Zhang et al. [2014]*. However, several works  
 553 (e.g. *Wang et al. [2015]*, *Abernathey and Haller [2018]*) using Lagrangian frameworks indicate  
 554 these Eulerian methods strongly overestimate the degree of eddy material transport. Additionally,  
 555 *Cetina-Heredia et al. [2019]* adopted Eulerian and Lagrangian approaches to highlight the potential  
 556 of eddies to impact the environment depends upon whether they maintain water inside or leak it.  
 557 In this study, we explored the relationship between eddy detection methods and coherent material  
 558 transport and quantitatively calculated the leakiness of Eulerian eddies.

559 An idealized eddy-resolving ocean basin, closely resembling the North Pacific ocean, was  
 560 simulated using MITgcm. More than 55 million Lagrangian particles were introduced into the  
 561 model and advected by 2D surface flow in the final 5 years. We identified Lagrangian coherent



490 **Figure 14.** Same as Figure 7, but for randomly selected (top panels) a fixed circle and (bottom panels) a  
 491 moving circle.



492 **Figure 15.** Bar diagram showing the ratio of leakage and intrusion after 30 days for RCLVs, overlapping SSH  
 493 eddies, non-overlapping SSH eddies, fixed circles, and moving circles. The black error bar indicates the one  
 494 standard deviation. The crossover day of leakage and intrusion is presented by the green dashed line. Specially,  
 495 RCLVs have zero leakage and intrusion for their coherent property.

562 eddies (also called RCLVs) in 30- and 90-day intervals by the method *Haller et al.* [2016]. In the  
 563 corresponding time interval, SSH eddies were detected from SSHA fields through the approach  
 564 proposed by *Faghmous et al.* [2015].

565 General statistical features of RCLVs were compared to those of SSH eddies. We found that  
 566 RCLVs have a much smaller coherent core than SSH eddies and are often enclosed by SSHA contours.  
 567 Specially, about 25% of RCLVs were found to be not located near a local peak of SSHA. We also  
 568 found that mean radius of all RCLVs (35.5 km) is approximately about half of the mean SSH eddy  
 569 radius (72.4 km). Both RCLVs and SSH eddies had similar westward propagation speed with  
 570 the latitude. Assuming SSH eddies could maintain coherence over their whole lifetimes, the zonal  
 571 coherent transport by RCLVs was around half of the transport by SSH eddies.

572 The principal focus and innovation of this paper was the calculation of material flux across  
 573 Eulerian eddy boundaries. The eddies were classified into three categories: overlapping RCLVs and  
 574 SSH eddies, non-overlapping SSH eddies, and non-overlapping RCLVs. Using Lagrangian particles,  
 575 we examined the processes of leakage and intrusion around overlapping and non-overlapping SSH

576 eddies. For 30-day overlapping SSH eddies, over their lifetimes, the materially coherent part is only  
577 about 25% of the total volume (recognized as RCLVs), while about 50% of initial water escapes into  
578 the background flow. The remaining 25% of water can still stay inside the SSH eddy boundary, but  
579 in the form of filaments outside the coherent core. After about 20 days, the intruded water exceeds  
580 the amount of initial water in SSH eddies, which provides an evidence that there is strong water  
581 exchange around SSH eddies. Strong leakage and intrusion are also found in 90-day overlapping  
582 SSH eddies. For non-overlapping SSH eddies, more water leakage (about 60%) occurs at a faster  
583 rate.

584 Guided by the number and radius of SSH eddies, fixed circles and moving circles were selected  
585 in random regions and time interval to provide a baseline against which to compare the SSH eddies.  
586 After 30 days, there was still about 18% and 35% of initial water surrounded by these artificial  
587 boundaries for fixed and moving cases. In particular, the leakage and intrusion trends of moving  
588 circles were quite similar to that of non-overlapping SSH eddies. These findings suggests that the  
589 material coherence properties of roughly 50% of SSH eddies are not significantly different from  
590 randomly selected pieces of ocean with the same size.

591 Some statistical works based on satellite altimetry (e.g. *Chelton et al.* [2011]; *Cheng et al.*  
592 [2014]; *Samelson et al.* [2014]) reported that the lifespans of SSH eddies range from several weeks  
593 to tens of weeks. However, *Abernathey and Haller* [2018] concluded that RCLVs uniformly live  
594 shorter than SSH eddies and they only identified 1 RCLV with lifetime of 270 days in the eastern  
595 Pacific over more 20 years, against the number of 2076 in the SSH eddy dataset (*Chelton et al.*  
596 [2011]). In this study, therefore, we excluded the long-lived eddies and focus on coherent eddies  
597 with lifetime shorter than 90 days. In addition, the most peculiar thing is that Lagrangian eddies are  
598 defined on specific time intervals (we used 30- and 90-day here). This “finite time” nature of the  
599 LAVD method does not allow us to trivially detect eddies with an unlimited duration. Our solution  
600 was searching for SSH eddies that live in the same time interval with RCLVs, which might cut a  
601 long-lived SSH eddy into different shorter-lived eddies. But, reconciling the lifetime of Lagrangian  
602 eddies and Eulerian eddies is still an ambiguous question.

603 Another limitation of the our results is the Lagrangian particles in the model only are advected  
604 by the 2D surface velocity. But, in reality, the coherent eddies are fully 3D structures with vertical  
605 motions result from a variety of mechanisms (*Gaube et al.* [2015]). Recent work by *Sinha et al.*  
606 [2019] found that vertical advection greatly increases by improving the temporal resolution of forcing  
607 fields and suggested that vertical motions may be underestimated in the coherent structures derived  
608 from temporally filtered velocities. The reason we neglect the vertical motions in this study is to  
609 create a relative fair condition to compare two different categories of eddies and examine the leakiness  
610 of SSH eddies, since SSH field does not contain the information of vertical motions. Future work is  
611 definitely required to uncover the complete image (horizontal and vertical structure) of Lagrangian  
612 eddies by deploying particles on isopycnals, extending this comparison from 2D to 3D next step.

613 The huge range of applications in the oceanography community and the availability of open-  
614 source algorithms impel us to choose SSH eddies as representative of Eulerian eddies in this study.  
615 However, the outermost closed contour of SSH is not the only one of criteria to define an eddy. The  
616 leakage ratio of Eulerian eddies we calculated here may vary slightly if a tighter SSH threshold or  
617 another Eulerian method (e.g. OW parameter; potential vorticity contour) is adopted. However,  
618 the strong water exchange across the boundaries suggest that the choice of thresholds or Eulerian  
619 variables will not change the fundamental shortcomings of Eulerian detection methods we mentioned  
620 before.

621 Though the limitations exist, the final conclusions from this study are clear: if one wishes to  
622 estimate material transport, a Lagrangian eddy detection algorithm is best, since Eulerian eddies are  
623 highly leaky. While Eulerian eddies may contain a materially coherent core, this core is identified  
624 well by the RCLV algorithm. But there are just as many Eulerian eddies with no materially coherent  
625 core. We see no obvious way to separate these two cases *a priori*, i.e. without also doing Lagrangian  
626 eddy detection.

627 However, the fact is that running a model with millions of Lagrangian particles and conducting  
 628 the identification remains a heavy computational task. The recent publication of an efficient La-  
 629 grangian Coherent Structure software package may mitigate this somewhat (`CoherentStructures.jl`;  
 630 *Karrasch and Schilling* [2019]). We are also in the process of compiling a global RCLV database  
 631 based on satellite altimetry, which should provide useful for future transport estimates.

### 632 Acknowledgments

633 Tongya Liu was supported by the National Natural Science Foundation of China (41730535,  
 634 41621064), the China Scholarship Council (NO. 201806320323). Ryan Abernathey was supported by  
 635 NSF Award OCE 15-53593. The computation in this research is carried out on Habanero shared high  
 636 performance cluster at Columbia University. The authors thank Wenda Zhang for the improvement  
 637 of Lagrangian eddy detection algorithm, and Choe E. Tae for suggestions on this manuscript. The  
 638 open source Eulerian eddy identification algorithm is from <https://github.com/jfaghm/OceanEddies>.  
 639 Quikscat wind data are available <https://winds.jpl.nasa.gov/missions/quikscat/>; World Ocean Atlas  
 640 2013 are available at <https://www.nodc.noaa.gov/OC5/indprod.html>; AVISO dataset can be found at  
 641 <http://www.aviso.altimetry.fr/en/home.html>.

### 642 References

- 643 Abernathey, R., and G. Haller (2018), Transport by lagrangian vortices in the eastern pacific, *Journal*  
 644 *of Physical Oceanography*, 48(3), 667–685.
- 645 Beron-Vera, F. J., M. J. Olascoaga, and G. Goni (2008), Oceanic mesoscale eddies as revealed by  
 646 lagrangian coherent structures, *Geophysical Research Letters*, 35(12).
- 647 Beron-Vera, F. J., Y. Wang, M. J. Olascoaga, G. J. Goni, and G. Haller (2013), Objective detection  
 648 of oceanic eddies and the agulhas leakage, *Journal of Physical Oceanography*, 43(7), 1426–1438.
- 649 Beron-Vera, F. J., M. J. Olascoaga, G. Haller, M. Farazmand, J. Triñanes, and Y. Wang (2015),  
 650 Dissipative inertial transport patterns near coherent lagrangian eddies in the ocean, *Chaos: An*  
 651 *Interdisciplinary Journal of Nonlinear Science*, 25(8), 087,412.
- 652 Cetina-Heredia, P., M. Roughan, E. Van Sebille, S. Keating, and G. B. Brassington (2019), Reten-  
 653 tion and leakage of water by mesoscale eddies in the east australian current system, *Journal of*  
 654 *Geophysical Research: Oceans*, 124(4), 2485–2500.
- 655 Chaigneau, A., A. Gizolme, and C. Grados (2008), Mesoscale eddies off peru in altimeter records:  
 656 Identification algorithms and eddy spatio-temporal patterns, *Progress in Oceanography*, 79(2-4),  
 657 106–119.
- 658 Chelton, D. B., R. A. Deszoeke, M. G. Schlax, K. El Naggar, and N. Siwertz (1998), Geographical  
 659 variability of the first baroclinic rossby radius of deformation, *Journal of Physical Oceanography*,  
 660 28(3), 433–460.
- 661 Chelton, D. B., M. G. Schlax, and R. M. Samelson (2011), Global observations of nonlinear  
 662 mesoscale eddies, *Progress in oceanography*, 91(2), 167–216.
- 663 Cheng, Y.-H., C.-R. Ho, Q. Zheng, and N.-J. Kuo (2014), Statistical characteristics of mesoscale  
 664 eddies in the north pacific derived from satellite altimetry, *Remote Sensing*, 6(6), 5164–5183.
- 665 Condie, S., and R. Condie (2016), Retention of plankton within ocean eddies, *Global Ecology and*  
 666 *Biogeography*, 25(10), 1264–1277.
- 667 Cox, M. D. (1985), An eddy resolving numerical model of the ventilated thermocline, *Journal of*  
 668 *Physical Oceanography*, 15(10), 1312–1324.
- 669 Dong, C., F. Nencioli, Y. Liu, and J. C. McWilliams (2011), An automated approach to detect oceanic  
 670 eddies from satellite remotely sensed sea surface temperature data, *IEEE Geoscience and Remote*  
 671 *Sensing Letters*, 8(6), 1055–1059.
- 672 Dong, C., J. C. McWilliams, Y. Liu, and D. Chen (2014), Global heat and salt transports by eddy  
 673 movement, *Nature communications*, 5, 3294.
- 674 dÓvidio, F., J. Isern-Fontanet, C. López, E. Hernández-García, and E. García-Ladona (2009),  
 675 Comparison between eulerian diagnostics and finite-size lyapunov exponents computed from  
 676 altimetry in the algerian basin, *Deep Sea Research Part I: Oceanographic Research Papers*, 56(1),

- 677 15–31.
- 678 Early, J. J., R. Samelson, and D. B. Chelton (2011), The evolution and propagation of quasigeostrophic  
679 ocean eddies, *Journal of Physical Oceanography*, *41*(8), 1535–1555.
- 680 Faghmous, J. H., I. Frenger, Y. Yao, R. Warmka, A. Lindell, and V. Kumar (2015), A daily global  
681 mesoscale ocean eddy dataset from satellite altimetry, *Scientific data*, *2*, 150,028.
- 682 Fox-Kemper, B., and D. Menemenlis (2008), Can large eddy simulation techniques improve  
683 mesoscale rich ocean models, *Ocean modeling in an eddying regime*, *177*, 319–337.
- 684 Frenger, I., M. Münnich, N. Gruber, and R. Knutti (2015), Southern ocean eddy phenomenology,  
685 *Journal of Geophysical Research: Oceans*, *120*(11), 7413–7449.
- 686 Froyland, G., C. Horenkamp, V. Rossi, and E. Van Sebille (2015), Studying an agulhas ring’s long-  
687 term pathway and decay with finite-time coherent sets, *Chaos: An Interdisciplinary Journal of*  
688 *Nonlinear Science*, *25*(8), 083,119.
- 689 Fu, L.-L., D. B. Chelton, P.-Y. Le Traon, and R. Morrow (2010), Eddy dynamics from satellite  
690 altimetry, *Oceanography*, *23*(4), 14–25.
- 691 Gaube, P., D. B. Chelton, R. M. Samelson, M. G. Schlax, and L. W. O’Neill (2015), Satellite  
692 observations of mesoscale eddy-induced ekman pumping, *Journal of Physical Oceanography*,  
693 *45*(1), 104–132.
- 694 Griffies, S. M., M. Winton, W. G. Anderson, R. Benson, T. L. Delworth, C. O. Dufour, J. P. Dunne,  
695 P. Goddard, A. K. Morrison, A. Rosati, et al. (2015), Impacts on ocean heat from transient  
696 mesoscale eddies in a hierarchy of climate models, *Journal of Climate*, *28*(3), 952–977.
- 697 Hallberg, R. (2013), Using a resolution function to regulate parameterizations of oceanic mesoscale  
698 eddy effects, *Ocean Modelling*, *72*, 92–103.
- 699 Haller, G. (2005), An objective definition of a vortex, *Journal of fluid mechanics*, *525*, 1–26.
- 700 Haller, G. (2015), Lagrangian coherent structures, *Annual Review of Fluid Mechanics*, *47*, 137–162.
- 701 Haller, G., and F. J. Beron-Vera (2013), Coherent lagrangian vortices: The black holes of turbulence,  
702 *Journal of Fluid Mechanics*, *731*.
- 703 Haller, G., A. Hadjighasem, M. Farazmand, and F. Huhn (2016), Defining coherent vortices objec-  
704 tively from the vorticity, *Journal of Fluid Mechanics*, *795*, 136–173.
- 705 Hausmann, U., and A. Czaja (2012), The observed signature of mesoscale eddies in sea surface  
706 temperature and the associated heat transport, *Deep Sea Research Part I: Oceanographic Research*  
707 *Papers*, *70*, 60–72.
- 708 Isern-Fontanet, J., E. García-Ladona, and J. Font (2003), Identification of marine eddies from  
709 altimetric maps, *Journal of Atmospheric and Oceanic Technology*, *20*(5), 772–778.
- 710 Jayne, S. R., and J. Marotzke (2001), The dynamics of ocean heat transport variability, *Reviews of*  
711 *Geophysics*, *39*(3), 385–411.
- 712 Karrasch, D., and N. Schilling (2019), Fast and robust computation of coherent lagrangian vortices  
713 on very large two-dimensional domains, *arXiv preprint arXiv:1907.08449*.
- 714 Klocker, A., and D. P. Marshall (2014), Advection of baroclinic eddies by depth mean flow, *Geo-*  
715 *physical Research Letters*, *41*(10), 3517–3521.
- 716 Kouketsu, S., H. Kaneko, T. Okunishi, K. Sasaoka, S. Itoh, R. Inoue, and H. Ueno (2016), Mesoscale  
717 eddy effects on temporal variability of surface chlorophyll a in the kuroshio extension, *Journal of*  
718 *oceanography*, *72*(3), 439–451.
- 719 Large, W. G., J. C. McWilliams, and S. C. Doney (1994), Oceanic vertical mixing: A review and a  
720 model with a nonlocal boundary layer parameterization, *Reviews of Geophysics*, *32*(4), 363–403.
- 721 Marshall, J., A. Adcroft, C. Hill, L. Perelman, and C. Heisey (1997a), A finite-volume, incompressible  
722 navier stokes model for studies of the ocean on parallel computers, *Journal of Geophysical*  
723 *Research: Oceans*, *102*(C3), 5753–5766.
- 724 Marshall, J., C. Hill, L. Perelman, and A. Adcroft (1997b), Hydrostatic, quasi-hydrostatic, and  
725 nonhydrostatic ocean modeling, *Journal of Geophysical Research: Oceans*, *102*(C3), 5733–5752.
- 726 Nencioli, F., C. Dong, T. Dickey, L. Washburn, and J. C. McWilliams (2010), A vector geometry-  
727 based eddy detection algorithm and its application to a high-resolution numerical model product  
728 and high-frequency radar surface velocities in the southern california bight, *Journal of Atmospheric*  
729 *and Oceanic Technology*, *27*(3), 564–579.

- 730 Okubo, A. (1970), Horizontal dispersion of floatable particles in the vicinity of velocity singularities  
731 such as convergences, in *Deep sea research and oceanographic abstracts*, vol. 17, pp. 445–454,  
732 Elsevier.
- 733 Peacock, T., G. Froyland, and G. Haller (2015), Introduction to focus issue: Objective detection of  
734 coherent structures.
- 735 Qiu, B., and S. Chen (2010), Interannual variability of the north pacific subtropical countercurrent  
736 and its associated mesoscale eddy field, *Journal of Physical Oceanography*, 40(1), 213–225.
- 737 Reynolds, O., A. W. Brightmore, and W. H. Moorby (1903), *Papers on Mechanical and Physical*  
738 *Subjects: The sub-mechanics of the universe*, vol. 3, The University Press.
- 739 Rio, M., S. Guinehut, and G. Larnicol (2011), New cnes-cls09 global mean dynamic topography  
740 computed from the combination of grace data, altimetry, and in situ measurements, *Journal of*  
741 *Geophysical Research: Oceans*, 116(C7).
- 742 Risien, C. M., and D. B. Chelton (2008), A global climatology of surface wind and wind stress  
743 fields from eight years of quikscat scatterometer data, *Journal of Physical Oceanography*, 38(11),  
744 2379–2413.
- 745 Samelson, R., M. Schlax, and D. Chelton (2014), Randomness, symmetry, and scaling of mesoscale  
746 eddy life cycles, *Journal of Physical Oceanography*, 44(3), 1012–1029.
- 747 Sinha, A., D. Balwada, N. Tarshish, and R. Abernathey (2019), Modulation of lateral transport by  
748 submesoscale flows and inertia-gravity waves, *Journal of Advances in Modeling Earth Systems*,  
749 11(4), 1039–1065.
- 750 Tarshish, N., R. Abernathey, C. Zhang, C. O. Dufour, I. Frenger, and S. M. Griffies (2018), Identifying  
751 lagrangian coherent vortices in a mesoscale ocean model, *Ocean Modelling*, 130, 15–28.
- 752 Wang, Y., M. J. Olascoaga, and F. J. Beron-Vera (2015), Coherent water transport across the south  
753 atlantic, *Geophysical Research Letters*, 42(10), 4072–4079.
- 754 Wang, Y., F. J. Beron-Vera, and M. J. Olascoaga (2016), The life cycle of a coherent lagrangian  
755 agulhas ring, *Journal of Geophysical Research: Oceans*, 121(6), 3944–3954.
- 756 Weiss, J. (1991), The dynamics of enstrophy transfer in two-dimensional hydrodynamics, *Physica*  
757 *D: Nonlinear Phenomena*, 48(2-3), 273–294.
- 758 Zhang, Z., W. Wang, and B. Qiu (2014), Oceanic mass transport by mesoscale eddies, *Science*,  
759 345(6194), 322–324.

Figure 1.



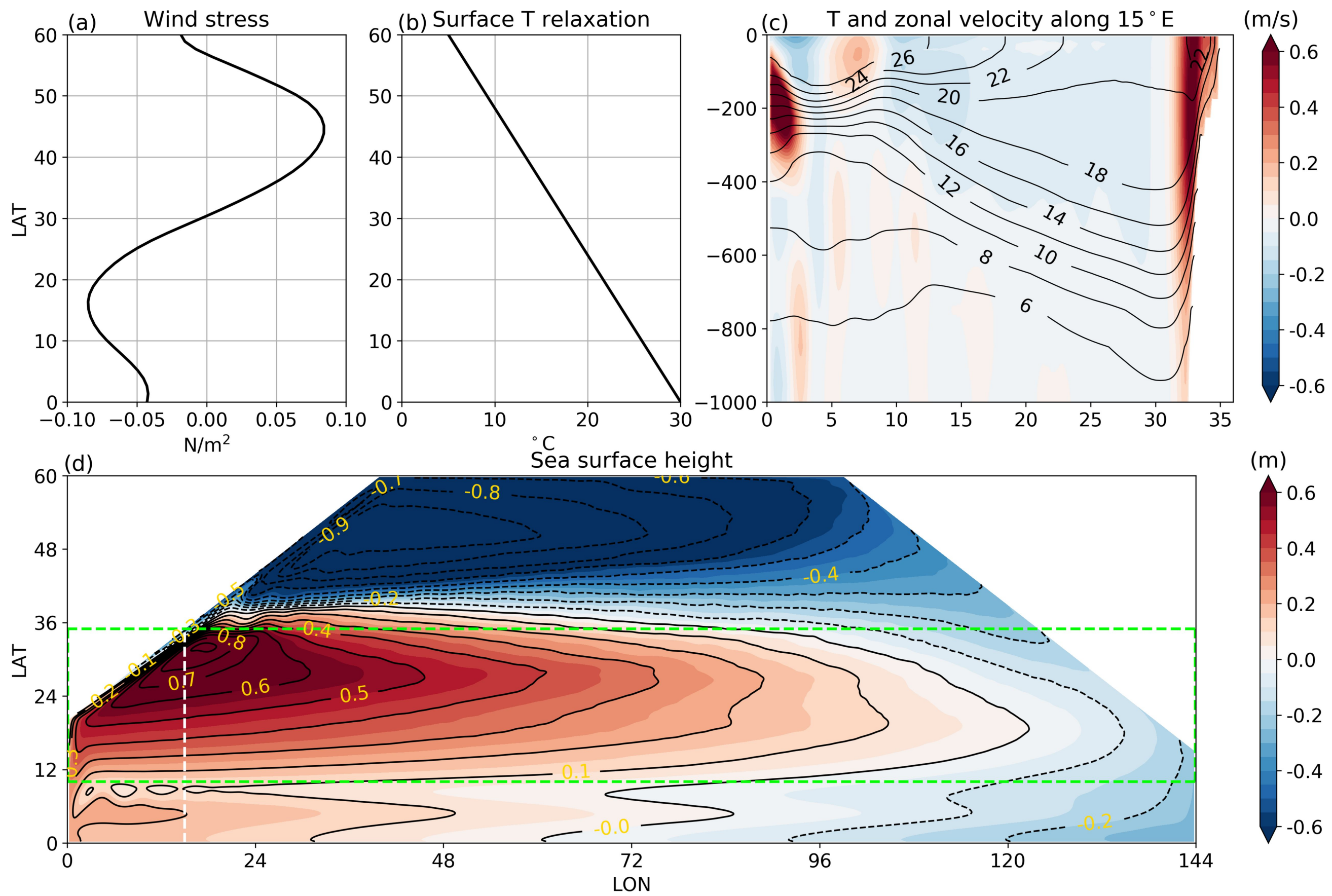


Figure 2.

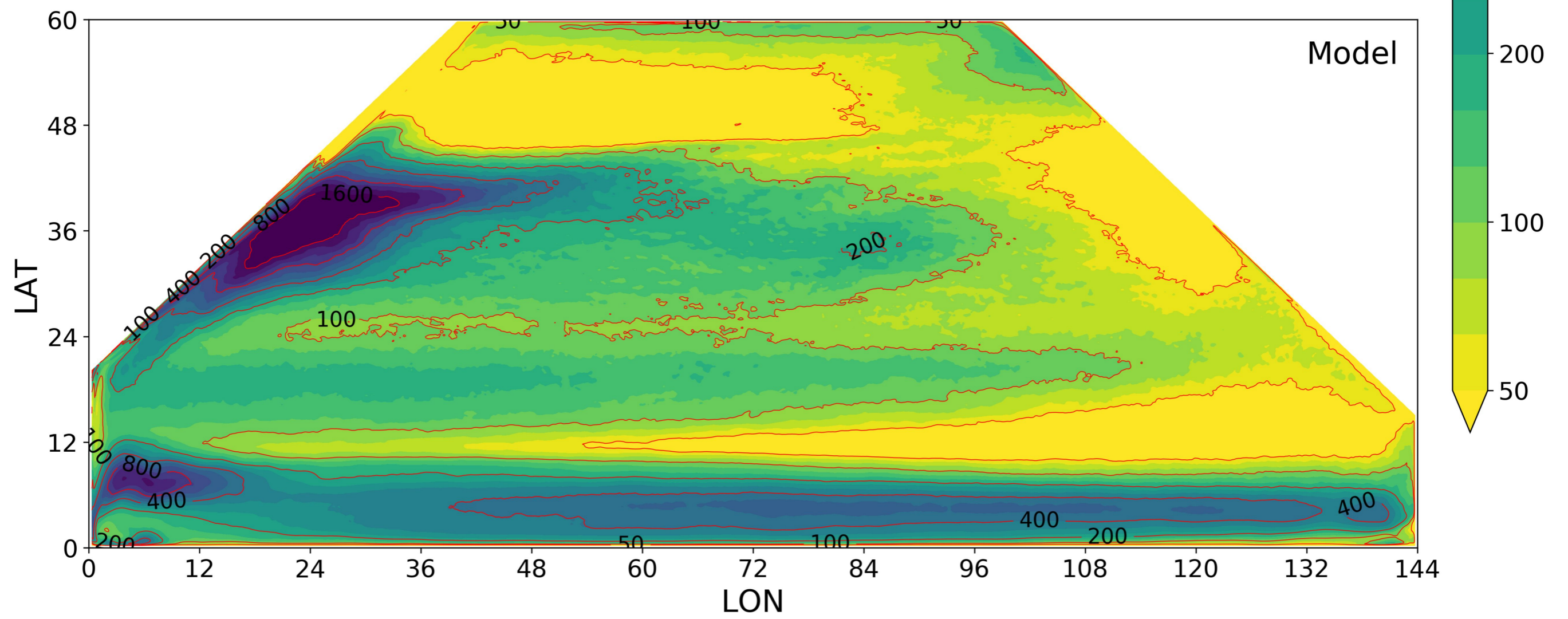
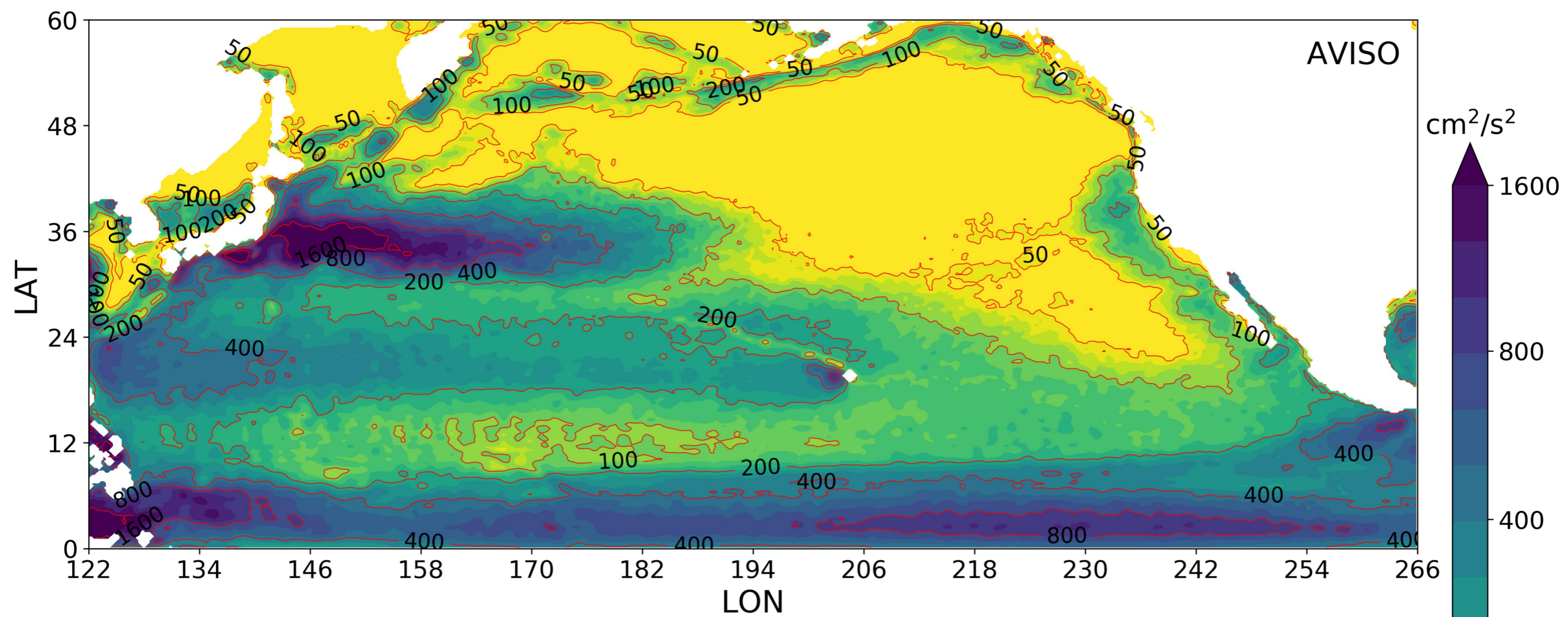


Figure 3.

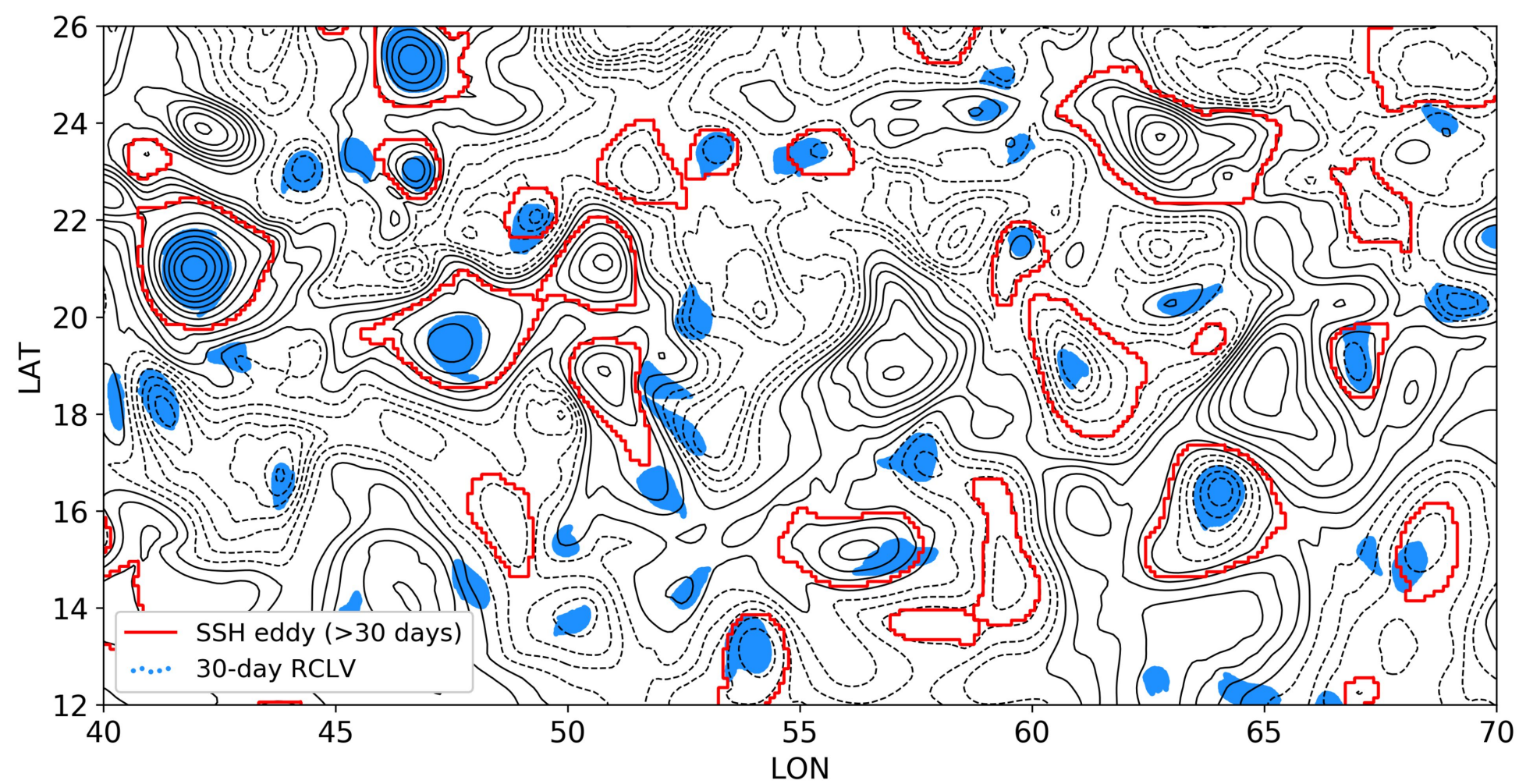


Figure 4.

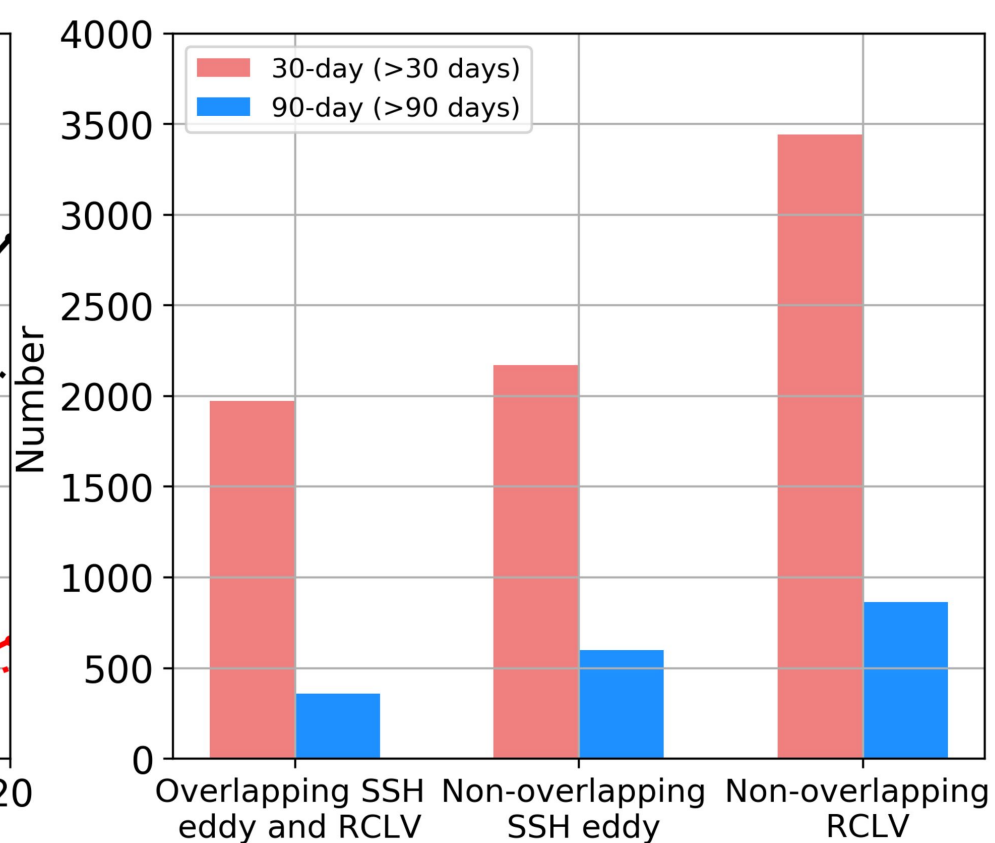
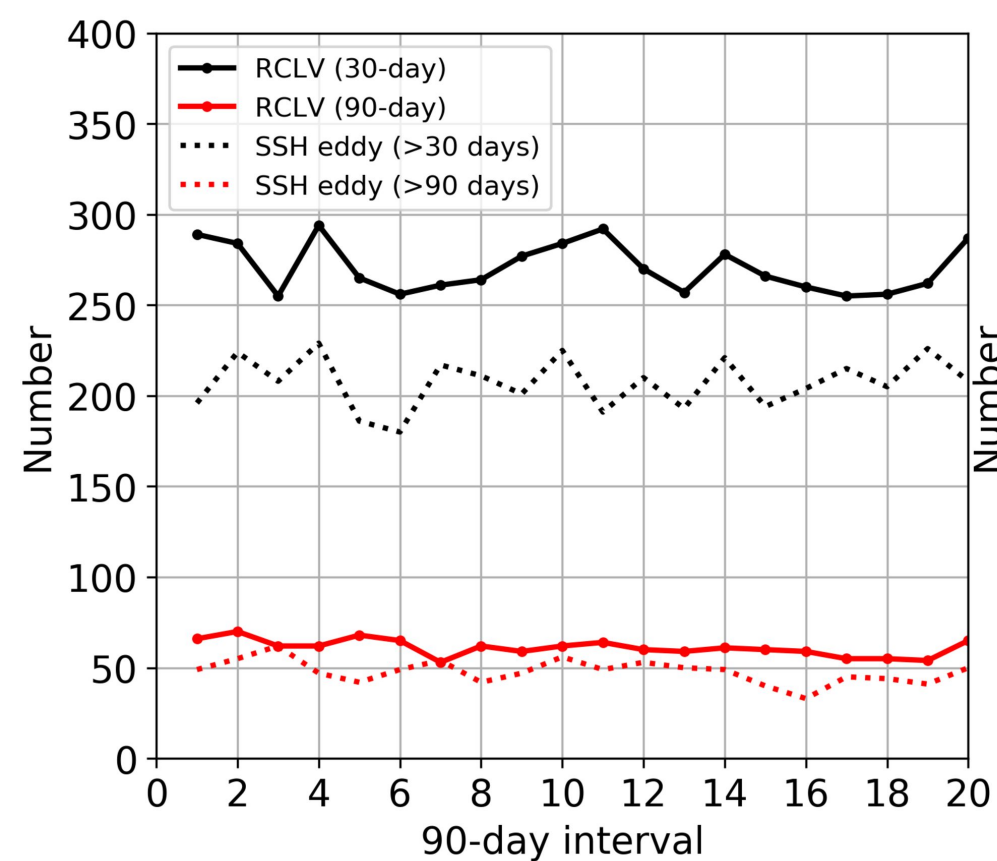
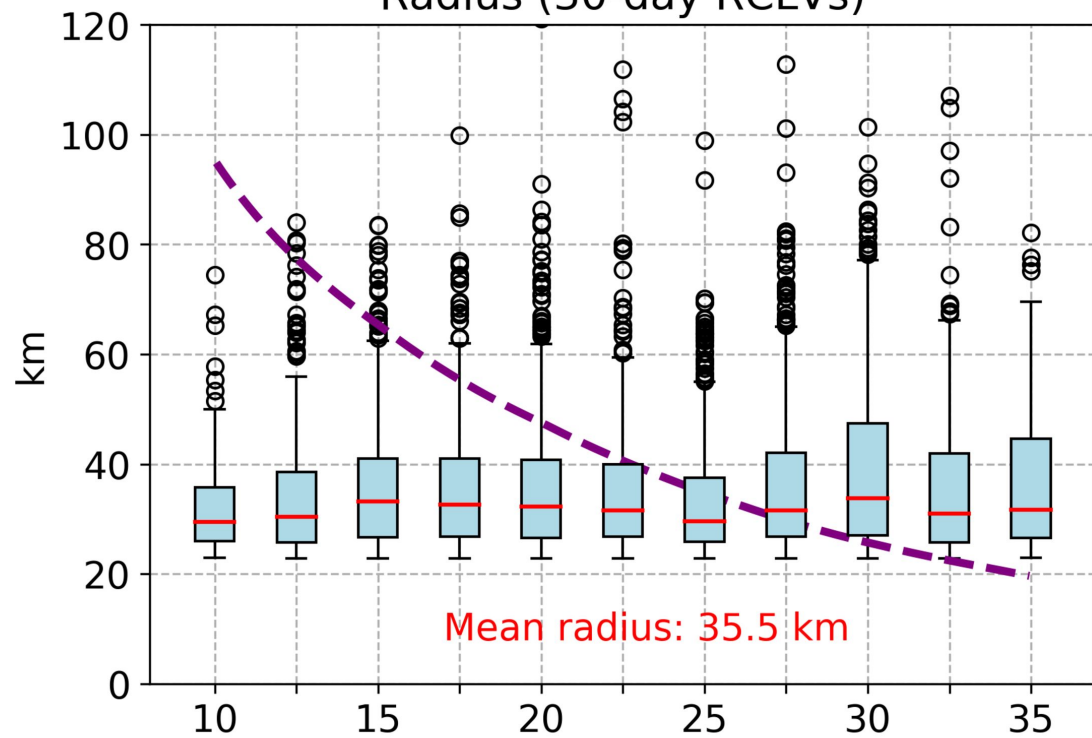


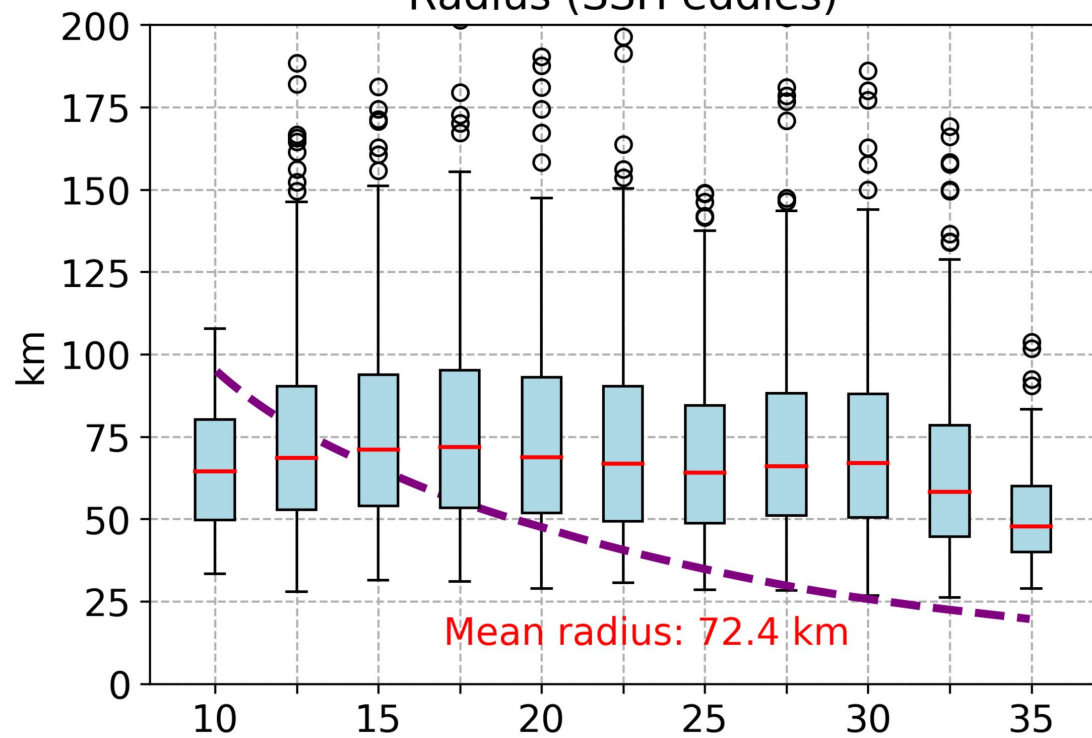
Figure 5.



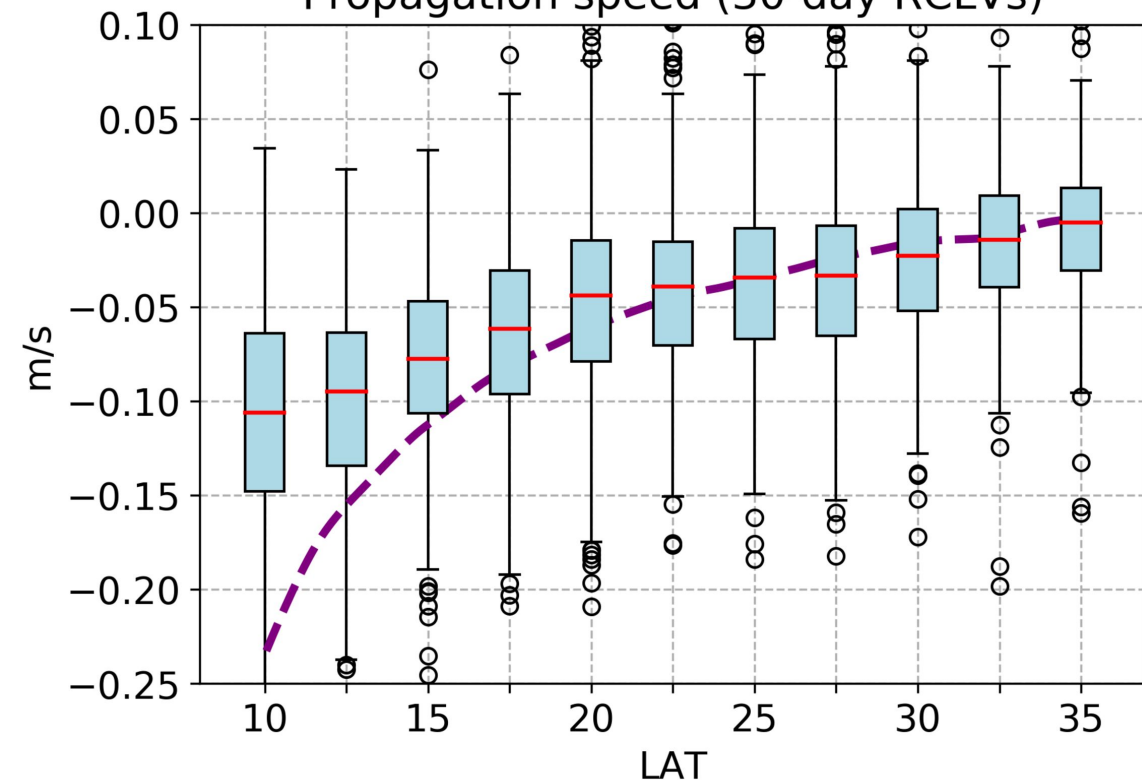
Radius (30-day RCLVs)



Radius (SSH eddies)



Propagation speed (30-day RCLVs)



Propagation speed (SSH eddies)

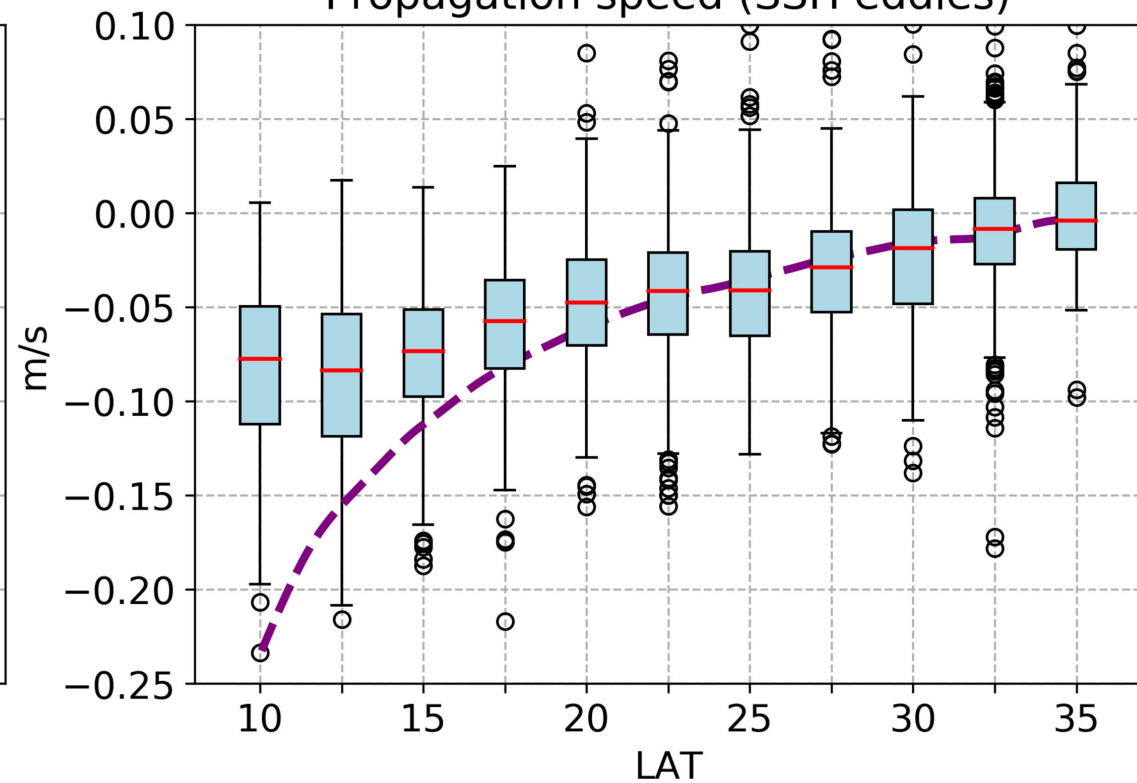


Figure 6.

# Zonally averaged zonal transport

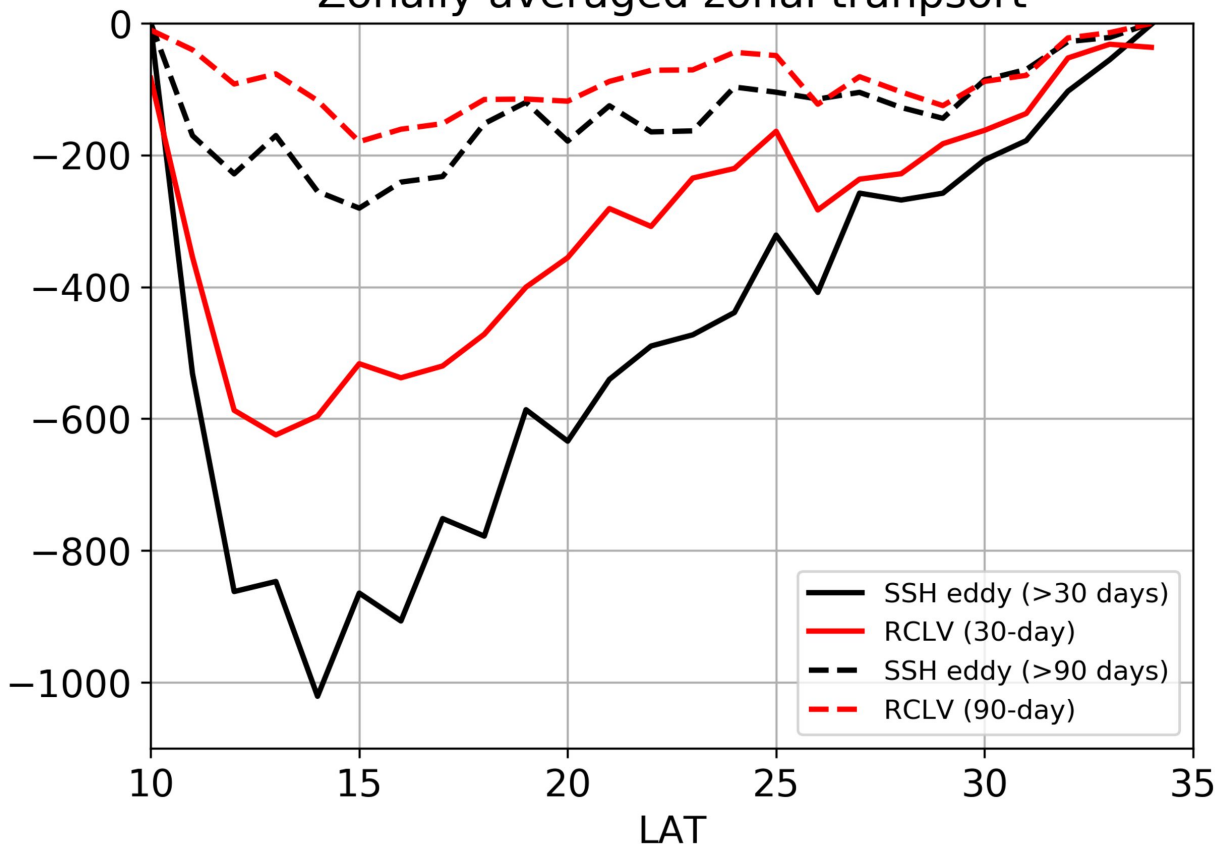


Figure 7.

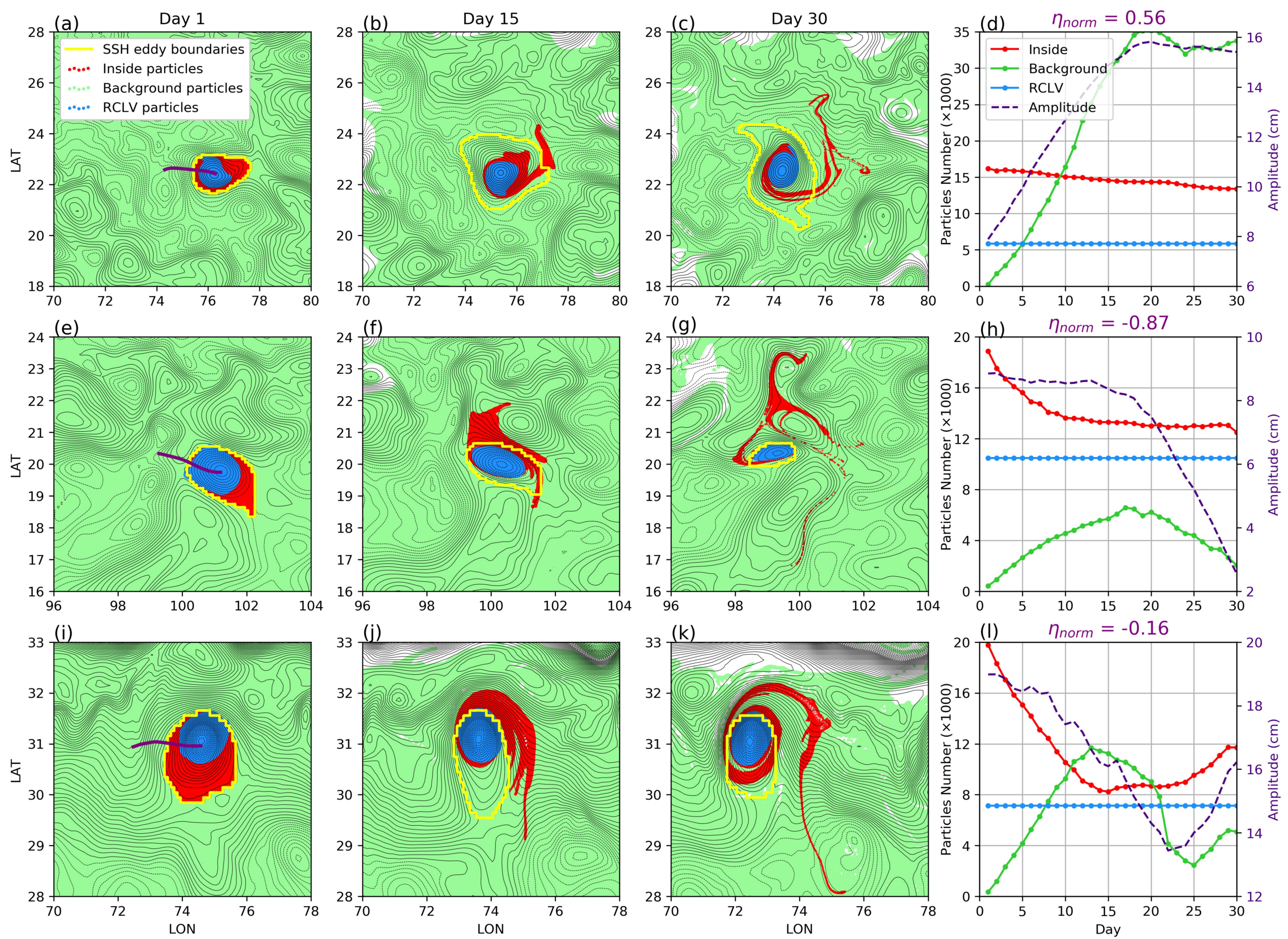
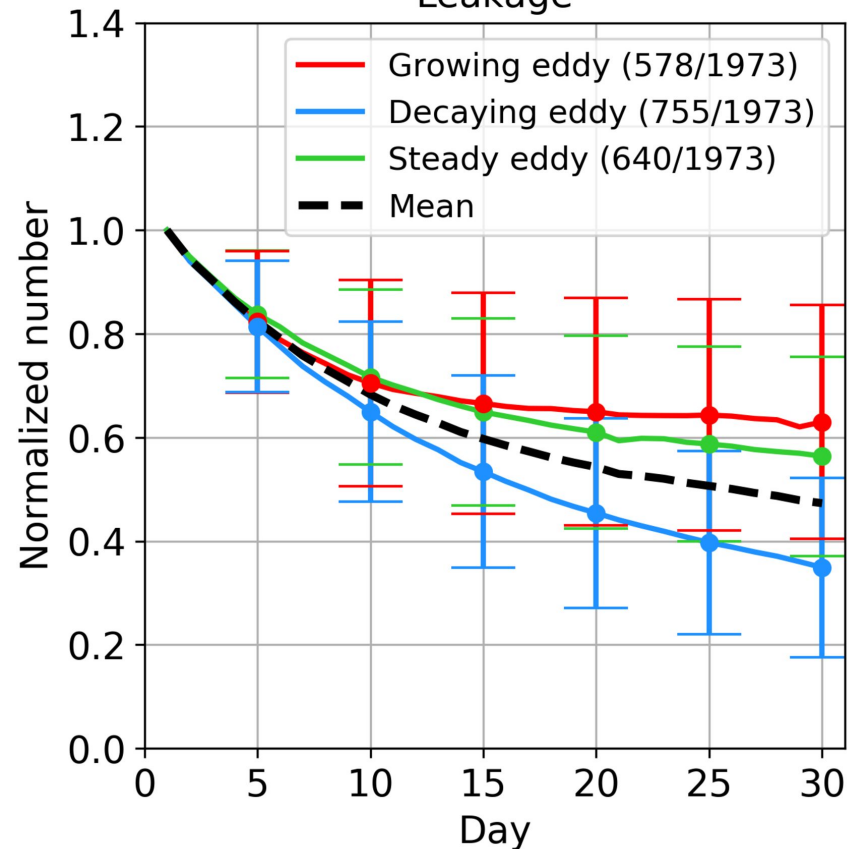
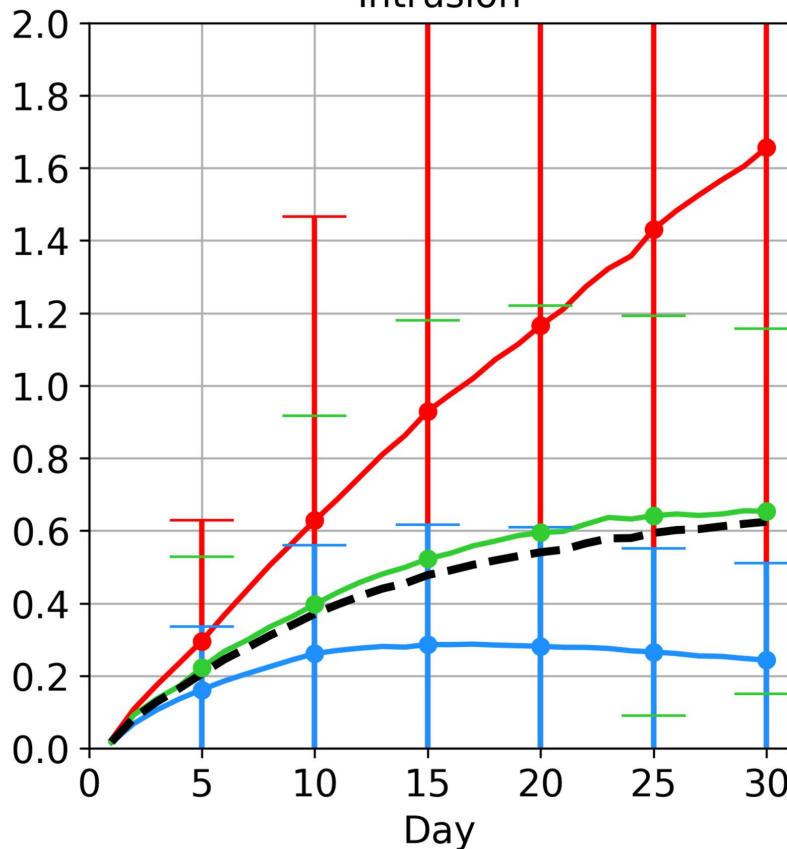


Figure 8.

Leakage



Intrusion



Comparison

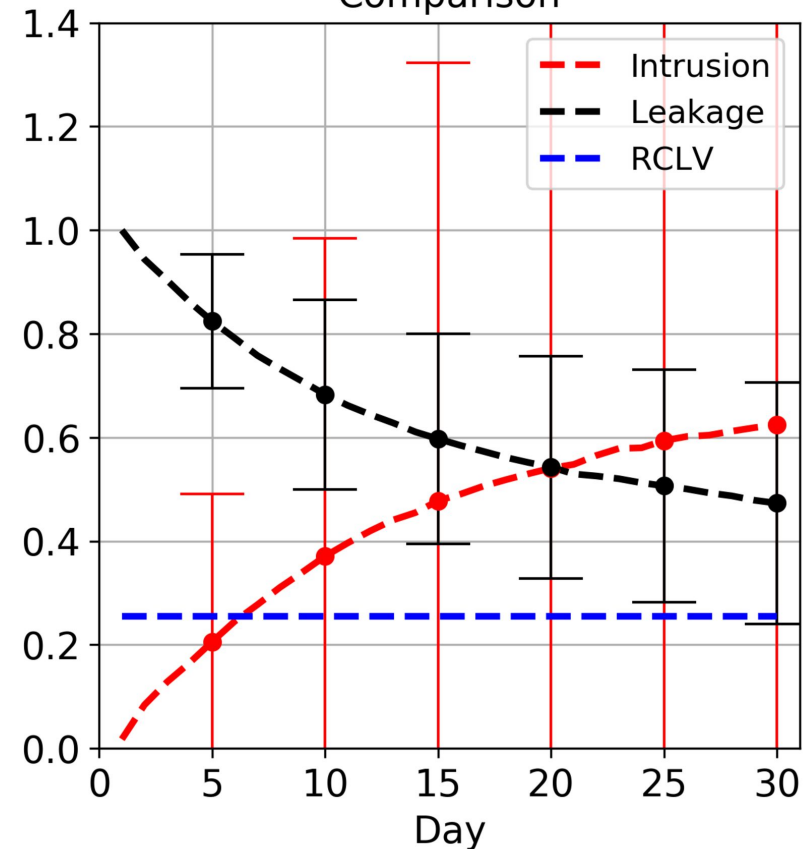


Figure 9.



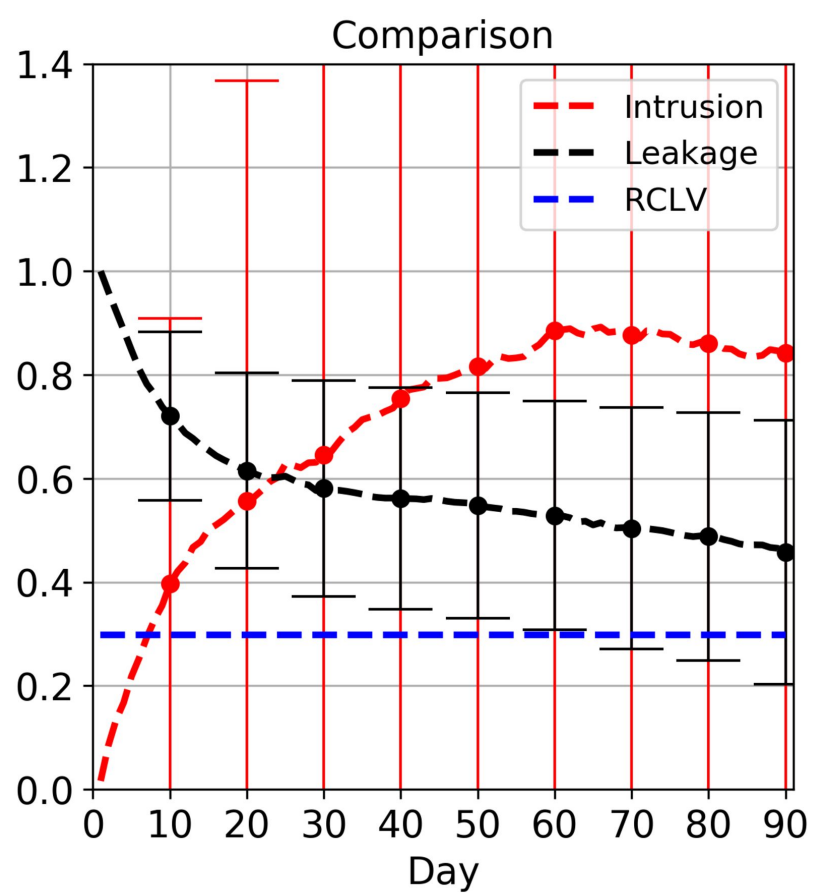
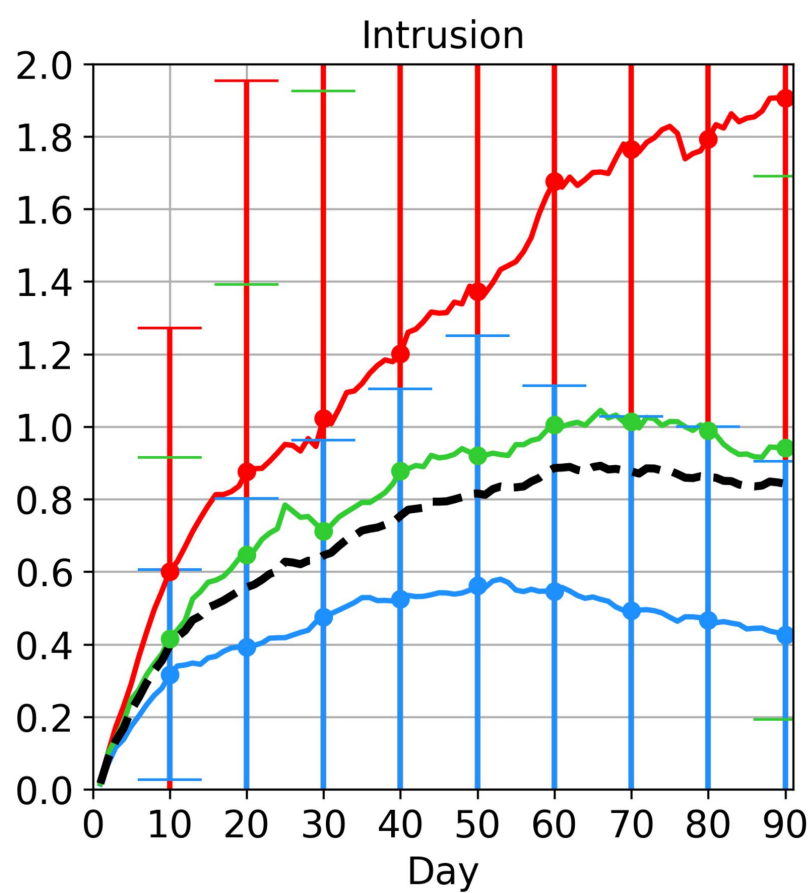
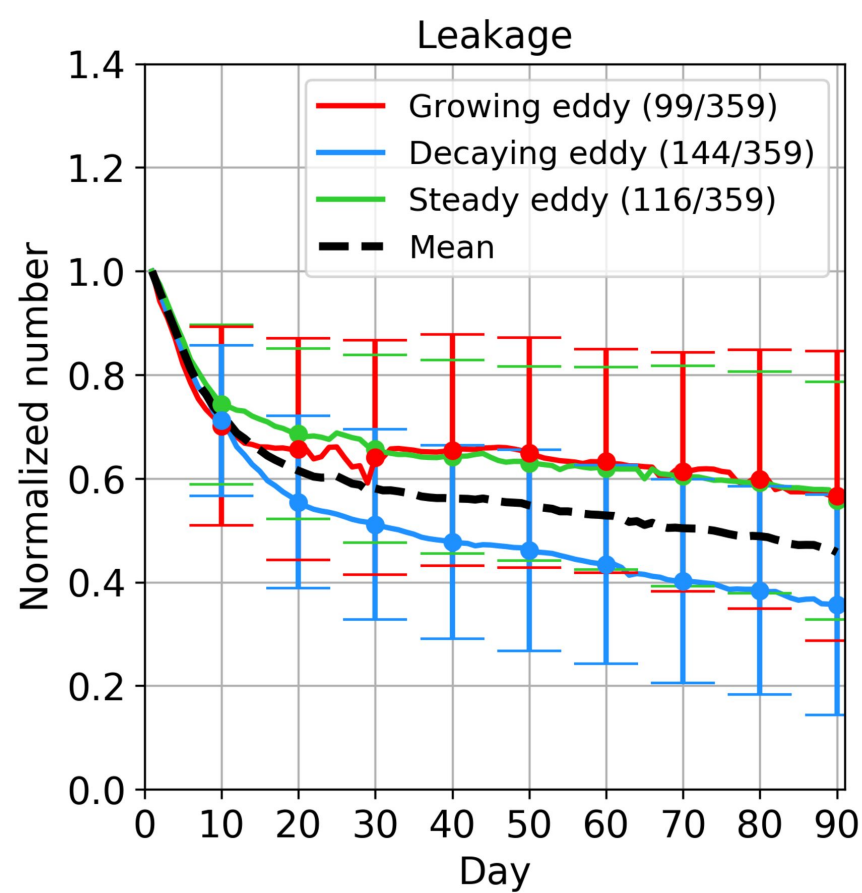
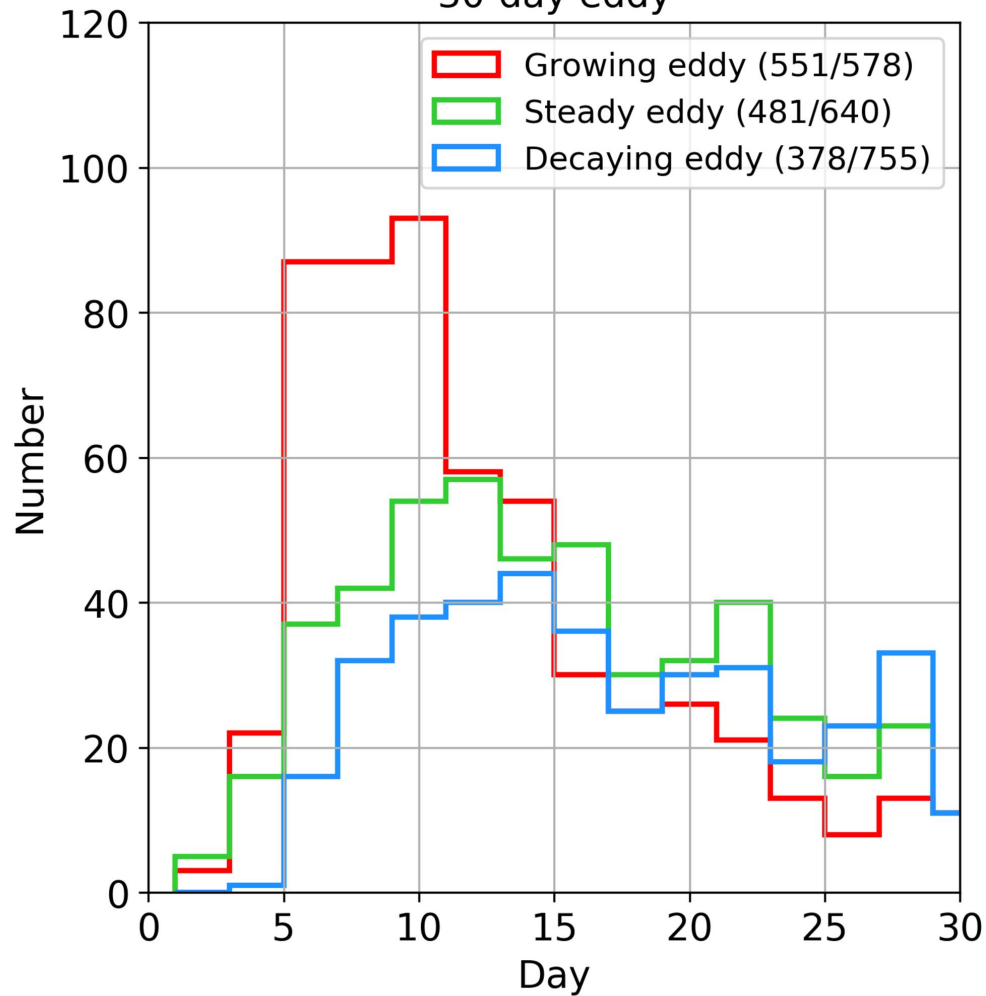


Figure 10.

30-day eddy



90-day eddy

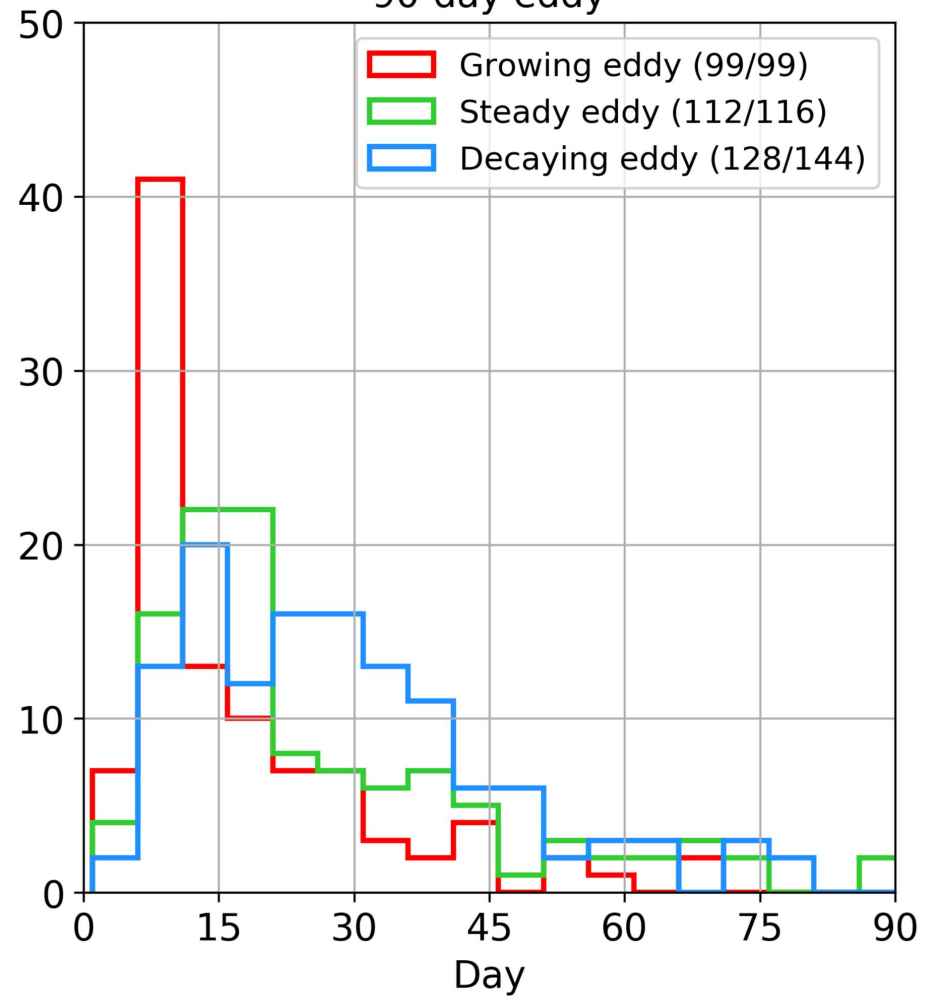


Figure 11.

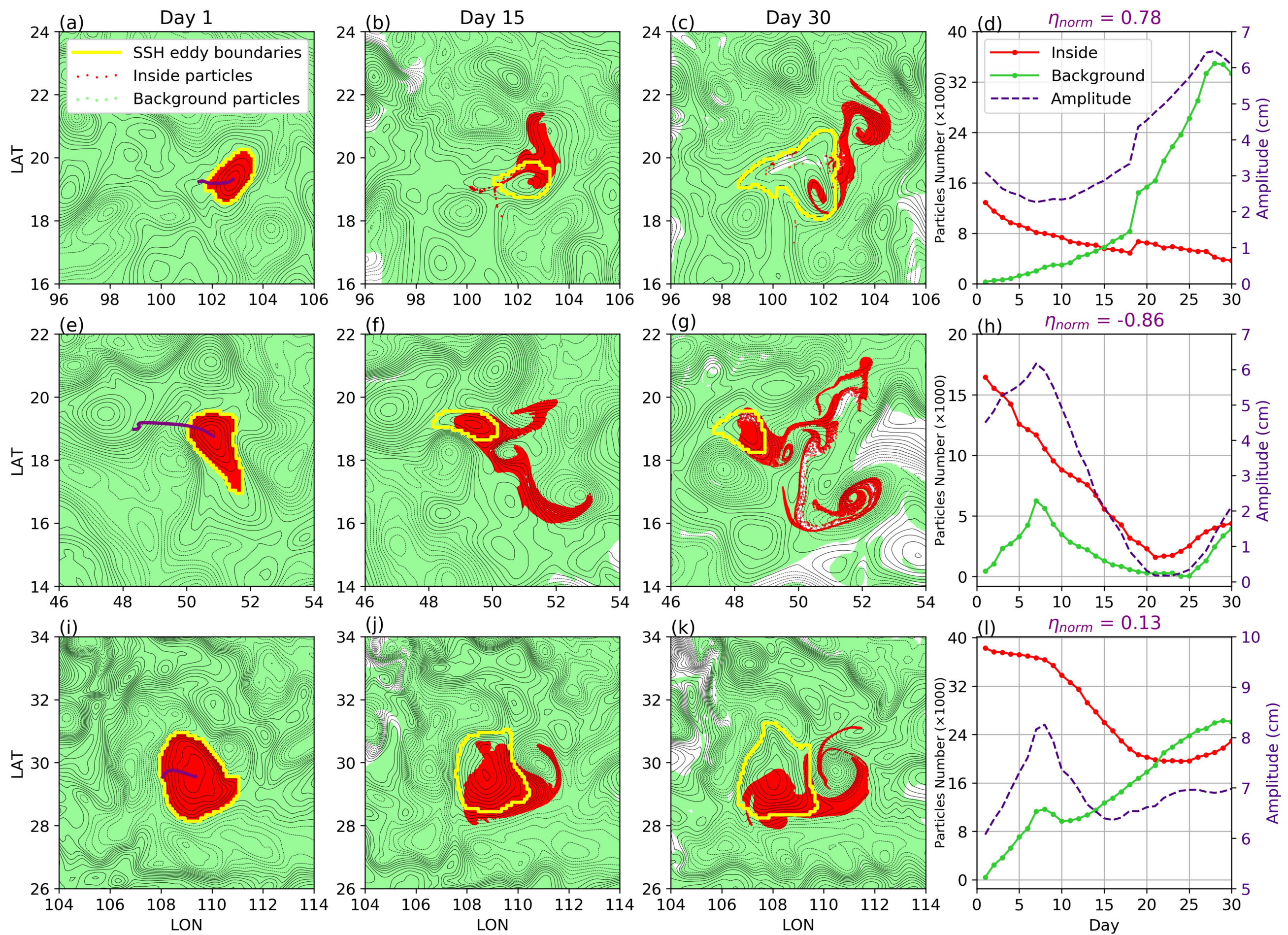


Figure 12.

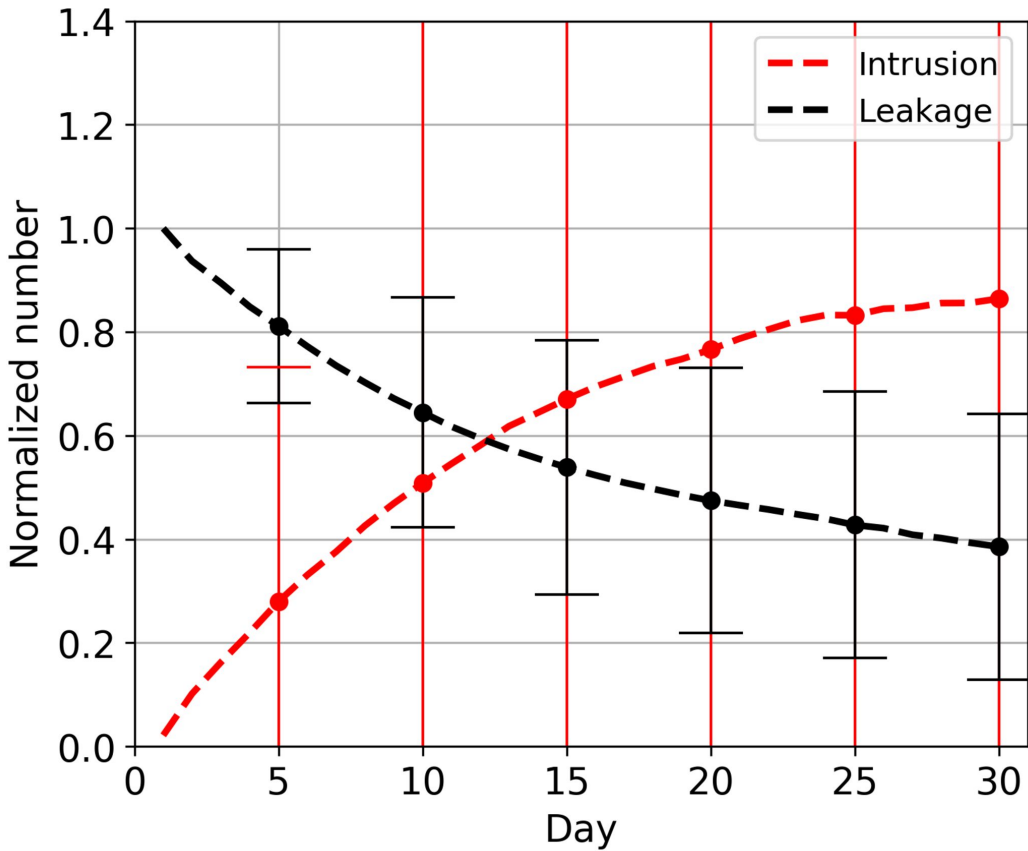
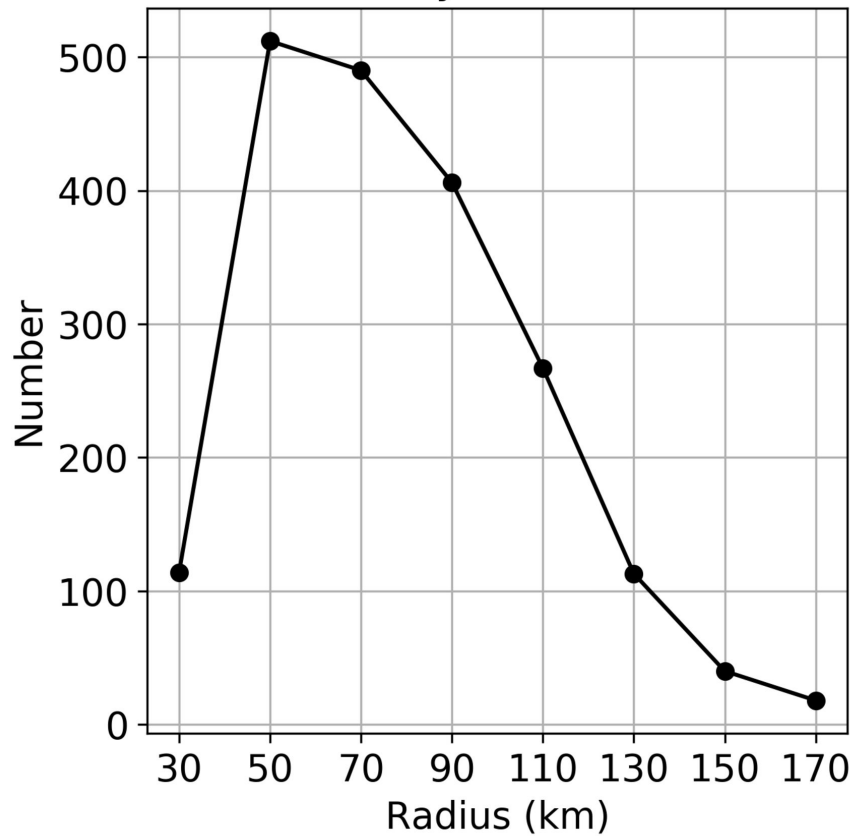


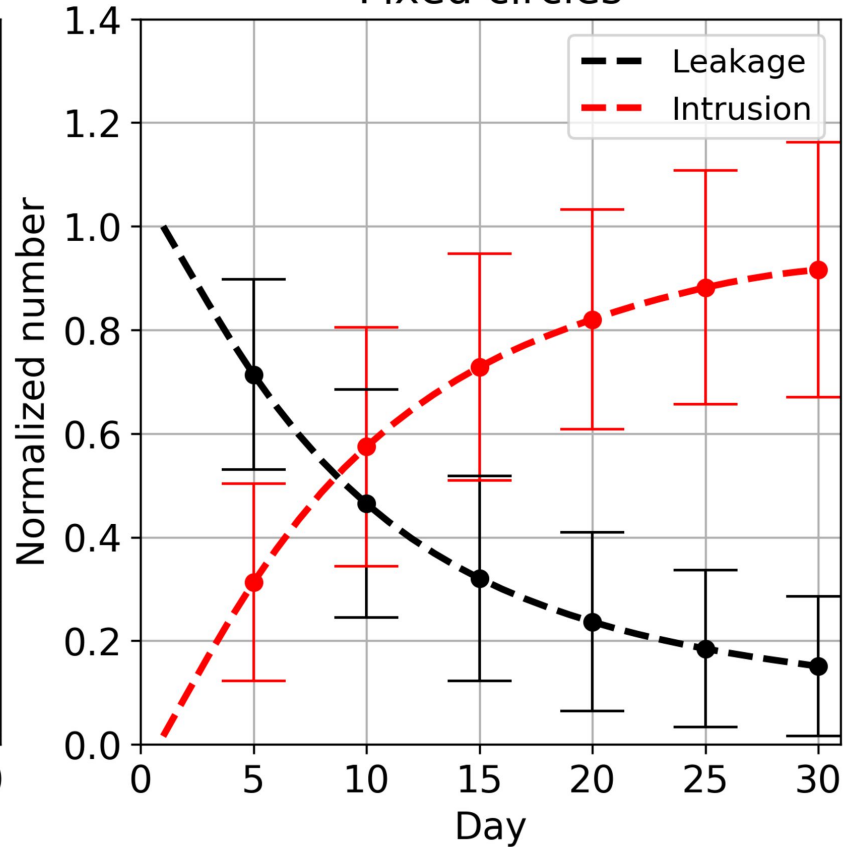
Figure 13.



Eddy number



Fixed circles



Moving circles

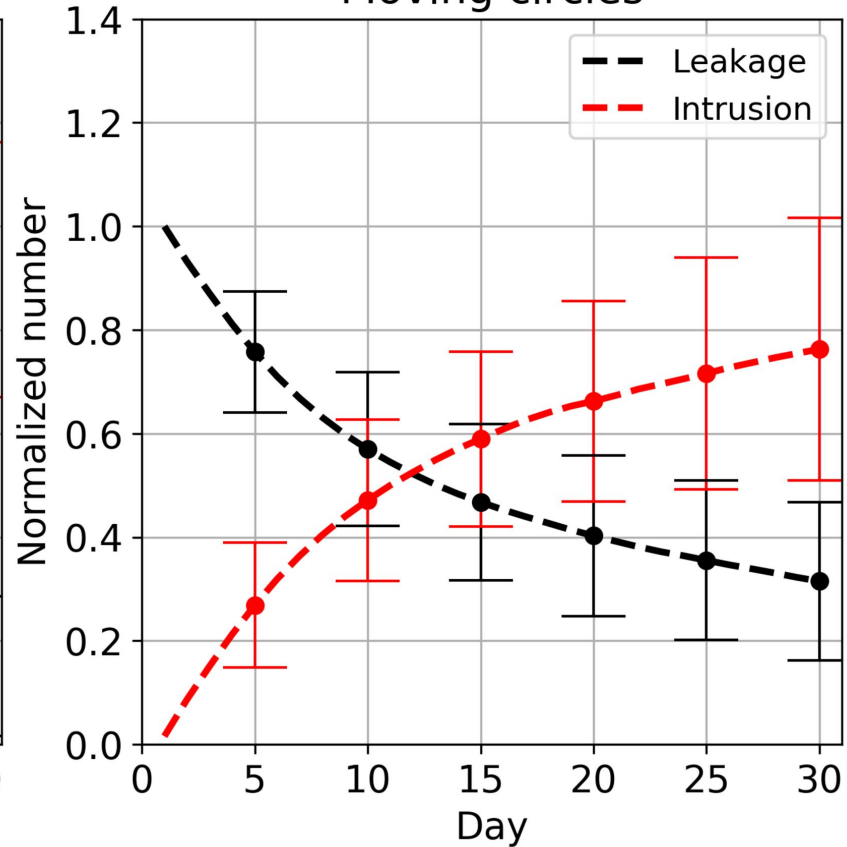


Figure 14.

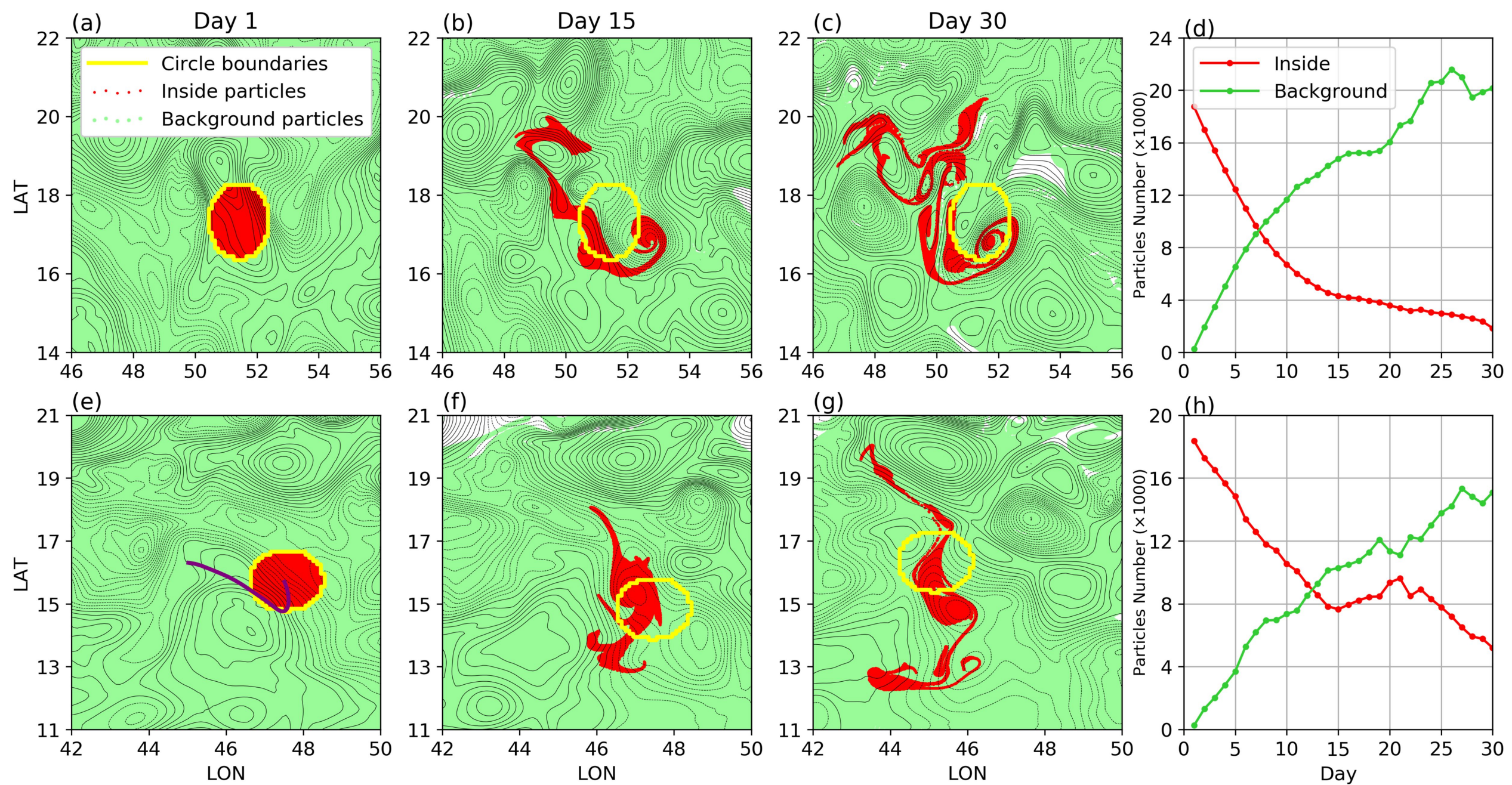


Figure 15.

